Computational Homogenization of Elastic-Viscoplastic Refractory Masonry with Dry Joints

Mahmoud Mahmoud Alaa Ali, Thomas Sayet, Alain Gasser, Eric Blond

Computational Homogenization of Elastic-Viscoplastic Refractory Masonry with Dry Joints

Mahmoud Ali *, Thomas Sayet, Alain Gasser †, Eric Blond

LaMé laboratory (EA 7494), Université d'Orléans, Université de Tours, INSA Centre Val de Loire, 8 rue Léonard de Vinci, 45072 Orléans, France

Correspondence: * mahmoud.ali@univ-orleans.fr, † alain.gasser@univ-orleans.fr

---

Abstract

Refractory masonry with dry joints is widely used in the steel-making industry for the linings of several high-temperature components (> 1500 °C) including steel ladles and furnaces. To properly optimize the design and performance of these linings, thorough numerical models that consider the presence of joints, joints closure and reopening and the nonlinear elastic-viscoplastic behaviour (creep and stress relaxation) of refractories at high temperature are required. The present study reports on the formulation, numerical implementation, and application of a homogenized multi-scale elastic-viscoplastic model for the simulation of refractory masonry linings with dry joints. Refractory bricks are considered to exhibit linear elasticity as well as rate-dependent plasticity. Four joint patterns are predefined based on the state of bed and head joints. The homogenized elastic-viscoplastic behaviour of each joint pattern is determined using finite element based nonlinear homogenization approach. The transition criterion between the four patterns are defined in terms of macroscopic stresses and strains. Verification of the developed homogenized constitutive laws is carried out by comparing the numerical results of the detailed micro models (brick and joints are considered) with the homogeneous equivalent material models. Furthermore, comparisons with experimental results of refractory masonry walls subjected to biaxial compression load at room and high temperature are carried out. Good agreements between the experimental and numerical results are obtained. Then, the validated models are employed to predict the mechanical behavior of refractory masonry structures subjected to different loading conditions. The present numerical model is able to simulate the orthotropic, compressible, rate-dependent homogenized behaviour

of mortarless refractory masonry structures, and accounts for joints closure and reopening due to loading and unloading.

Keywords: nonlinear homogenization, computational homogenization, refractories, masonry, creep, modelling

Nomenclature

Subscripts

b	Brick
bed	Bed joint
d	Deviatoric
eq	Equivalent
$head$	Head joint
$i,\ j,\ k,\ l$	Indices of the dimension
UC	Periodic unit cell
$x,\ y,\ z$	Coordinates

Greek Letters

ν	Poisson's ratio of the bulk material
$\overline{\overline{\dot{\varepsilon}}}^{\,\mathrm{vp}}$	2nd order local viscoplastic strain rate tensor
$\overline{\overline{\Sigma}}$	2nd order macroscopic stress tensor
$\overline{\overline{\sigma}}$	2nd order local stress tensor
$\overline{\overline{\sigma}}_d$	2nd order local deviatoric stress tensor
$\overline{\overline{\varepsilon}}^{\,\mathrm{t}}$	2nd order local total strain tensor
$\overline{\overline{\varepsilon}}^{\,\mathrm{e}}$	2nd order local elastic strain tensor
$\overline{\overline{\varepsilon}}^{\,\mathrm{vp}}$	2nd order local viscoplastic strain tensor
Σ_{eq}	Macroscopic equivalent stress
σ_{eq}	Local equivalent stress
Σ_{ij}	Components of macroscopic stress tensor
σ_{ij}	Components of local stress tensor
$\widetilde{\nu}$	Macroscopic or effective Poisson's ratio

Roman Letters

$\overline{u}$	Displacement vector
$\overline{X}$	Position vector
$\overline{\overline{\overline{\overline{C}}}}^{\,\mathrm{e}}$	4th order macroscopic or effective elastic stiffness tensor
$\overline{\overline{\overline{\overline{N}}}}$	4th order viscoplastic localization tensor

$\overline{\overline{\dot{E}}}^{\,vp}$ 2nd order macroscopic steady state viscoplastic strain rate

$\overline{\overline{E}}^{\,t}$ 2nd order macroscopic total strain tensor

$\overline{\overline{I}}$ 2nd order identity tensor

$\widetilde{E}$ Macroscopic or effective Young's modulus

$\widetilde{G}$ Macroscopic or effective shear modulus

A Creep power law multiplier

d_b Brick depth

E_{ij} Components of macroscopic strain tensor

g_0 Initial thickness of dry joints

g_{bed} Instantaneous thickness of bed joints

g_{head} Instantaneous thickness of head joints

h_b Brick height

l_b Brick width

n Creep stress exponent

T Temperature

V_{UC} Periodic unit cell volume

Y Young's modulus of the bulk material

$\dot{E}_{eq}^{vp}$ Macroscopic equivalent viscoplastic strain rate

Superscripts

e Elastic

t Total

vp Viscoplastic

1 Introduction

Refractory masonry with dry joints is extensively used for the linings of several high temperature components such as steel ladles, furnaces and rotary kilns due to their high thermal, mechanical and chemical stability, good thermo-mechanical and thermo-chemical properties [1–5]. When used in steel ladles, they are subjected to high thermal gradients, thermal shock, cyclic thermal heating and cooling, high thermo-mechanical stresses, slag attack, and harsh chemical environment [6–11]. Therefore, the lifespan of steel ladles internal linings is very short (several castings). Moreover, the design and optimization of these linings is still an engineering challenge due to the complex interaction between thermal fields, chemistry and the nonlinear mechanical behaviour of refractories at high temperature [1, 6, 12].

In a typical industrial scale steel ladle, the internal linings are built with dry joints masonry (also called mortarless masonry). Thousands of refractory bricks are arranged periodically. Between the contact surfaces of the bricks, there are small gaps called dry joints. The macroscopic mechanical behaviour of these structures is orthotropic, nonlinear and different from the behaviour of the material of the bricks due to the following reasons: first, material discontinuity introduced by the presence of joints, and second, joints closure and reopening caused by cyclic loading and unloading [13–15]. To properly optimize the design and performance of these linings, rigorous numerical models are required especially when experimental work remains a challenging topic due to technical complexities and severe working conditions. The numerical model should consider the orthotropic and nonlinear behaviour of the linings at high temperature and should be efficient in terms of computational time and cost to enable full scale structural modelling of the linings.

However, most of previous studies on mortarless masonry typically focused on masonry used in civil structures (usually operates at room temperature) [16–24]. Therefore, the bricks are considered to exhibit isotropic linear elasticity. For example, several experimental and numerical studies are carried out to investigate the impact of contact surfaces roughness on the contact area between the bricks [16, 18] or load bearing capacity of the wall [25]. In

these studies, the micro finite element modelling (FEM) approach is adopted (i.e. bricks and joints are considered and only few bricks and joints are used as a physical model of the problem). Also, limit analysis and discrete element modelling of the collapse mechanism of masonry walls subjected to in-plane and out-of-plane loading conditions can be found in the literature [17, 19, 26–29]. It should be noted that the micro FEM approach is only suitable for modelling few bricks and joints because considering all the bricks and joints of a wall (hundreds of bricks) leads rapidly to too expensive computational costs and solution convergence problems.

In the case of refractory masonry, very limited number of studies could be found in the literature. Room and high temperature compression tests on two refractory bricks were carried out to investigate the impact of applied stress level on the gradual closure of joints and the contact area between the bricks [30, 31]. It has been found that the contact area between the bricks increases with the increase of the applied compression stress. Furthermore, dry joints close gradually (i.e. a decrease in joint thickness) with the gradual increase of the applied stress. With regard to numerical studies, Hou et al. [32] developed a 2D micro FE model to investigate the effect of linings thickness and material properties on the thermo-mechanical behaviour of steel ladle refractory linings. Due to the selected micro FEM approach, only 2D cut of few bricks and one joint is considered. Nguyen et al. [14] developed and validated a homogeneous equivalent material model, by replacing the bricks and joints with an equivalent material, for the simulation of mortarless refractory masonry structures. The bricks are considered to obey isotropic linear elasticity. The model considers the influence of joints closure on the homogeneous mechanical response of the structure. Their results indicate that the macroscopic behaviour of the masonry structure is orthotropic and nonlinear due to gradual closure of joints. It should be noted that the macroscopic model developed by Nguyen et al. [14] can be used to simulate large scale structures, such as steel ladles and furnaces, with reasonable computational costs.

From the above discussion, it could be inferred that most of previous studies on masonry with dry joints focus on civil structure masonry using micro FEM approach and consider elastic behaviour of the bricks. However, these models are not suitable to model large sized

structures such as steel ladles and furnaces. In addition, only one multi scale numerical model has been developed in the literature and it is suitable to simulate only the elastic or thermoelastic behaviour of the masonry. At high temperature, elastic models usually leads to overestimation of stress levels due to the elastic viscoplastic behaviour of refractories at high temperature [1, 15]. More studies to understand the effects of joints, joints closure and reopening combined with viscoplasticity on the mechanical behaviour of refractory masonry linings at high temperature are required.

The present paper aims at performing computational nonlinear homogenization of elastic viscoplastic mortarless refractory masonry structures and developing a multi scale numerical model for their simulation. The developed model is efficient in terms of computational cost as it replaces all the bricks and joints with an elastic viscoplastic homogeneous equivalent material model. The present work is an extension of the previous work developed by Nguyen et al. and Ali et al. [14, 15]. As compared to the work in the literature [14, 15], the addition of viscoplasticty to the developed multi scale numerical model promotes better understanding of the nonlinear mechanical behaviour of refractory masonry structures at high temperature and, therefore, assists in the optimization of their design and performance.

The present paper is organized as following: in section 2, description of the mortarless refractory masonry structure is presented. In section 3, periodic nonlinear computational homogenization of the refractory mortarless masonry structure and identification of the effective elastic and viscoplastic parameters are presented and discussed. Verification of the developed models and results of masonry structures subjected to different loading cases are presented and discussed in section 5. Key findings of the present study and conclusions are given in section 6.

2 Mortarless masonry structure

In the present study, the mortarless refractory masonry structure illustrated in figure 1 is considered. The height and diameter of a typical industrial steel ladle are around 5 and 4.5 m, respectively [15]. The internal linings (also called working lining) of the ladle

are built up from thousands of tapered shape refractory bricks. However, for the sake of simplicity, cuboid bricks are considered in the present study. Bricks with height h_b, width l_b and depth d_b are periodically arranged in running bond texture. Dry joints with initial thickness ($g_0 << h_b,\ l_b,\ d_b$) are separating the bricks from each other. The dimensions of the brick are: $l_b = 124\ mm,\ h_b = 76\ mm,\ d_b = 185\ mm$, and the initial thickness of the joints is $0.1\ mm$. Often, these joints are resulting from the surface unevenness, shape and dimensions errors of the bricks during production. However sometimes, for instance rotary kiln and blast furnace, the joints are designed by attaching cardboard spacers to the bricks during the installation to compensate for thermal expansion effects.

Two types of joints are defined on the basis of their orientation: bed joints with initial thickness $g_{0,bed}$ (horizontal joints) and head joints with initial thickness $g_{0,head}$ (vertical joints). Under cyclic thermal heating and cooling or mechanical loading and unloading, these joints can close and reopen. It should be noted that the mechanical response of mortarless masonry structures varies with the closure and reopening of joints. Previous experimental studies show that the stiffness of mortarless masonry structure increases with the closure of joints [30, 31]. This phenomenon should be considered when developing thorough numerical models for the simulation of mortarless masonry linings.

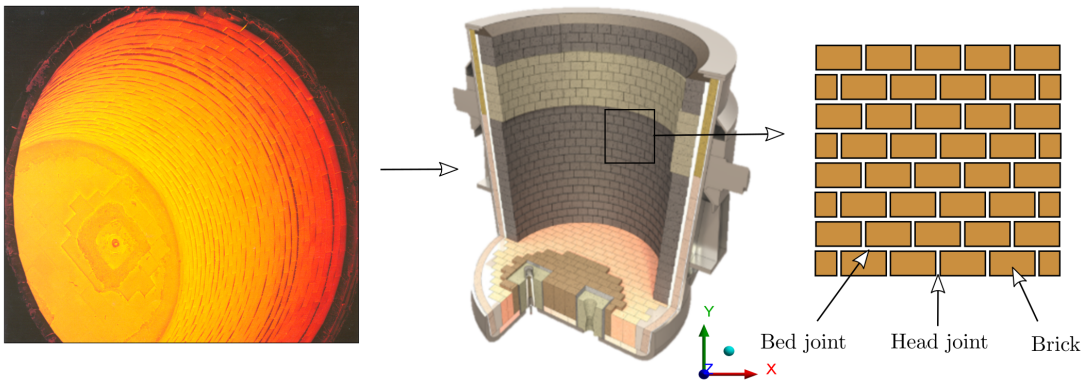

Figure 1: (a) Steel ladle lined with mortarless refractory masonry [33]. (b) Schematic of mortarless masonry wall showing the periodically arranged bricks and the gaps between them. Vertical gaps are called head joints and horizontal gaps are called bed joints.

For the purpose of considering the impact of joints closure and reopening on the homogenized elastic-viscoplastic behaviour of mortarless masonry structures, four possible

joint patterns are predefined (see figure 2). Each pattern is defined based on the state of both bed and head joints (i.e. open or closed) and represents different periodic masonry structure with different equivalent behaviour. The four joint patterns are as follows [14]:

1. Pattern C: head and bed joints are closed (all joints are closed).
2. Pattern B: bed joints are closed, while head joints are open.
3. Pattern H: head joints are closed, while bed joints are open.
4. Pattern O: head and bed joints are open (all joints are open).

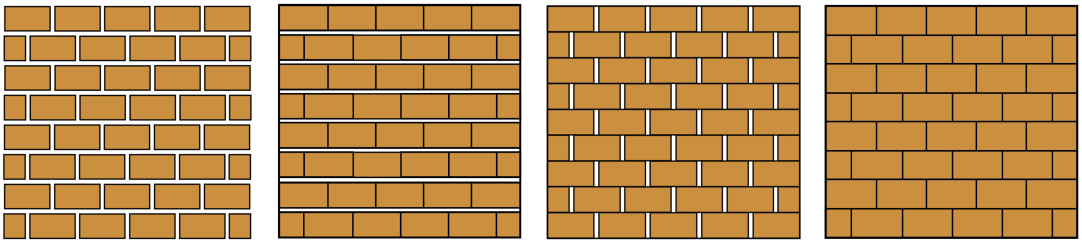

Figure 2: Schematics of possible joint patterns of mortarless refractory masonry structure (a) pattern O, (b) pattern H, (c) pattern B, and (d) pattern C. The four joint patterns are defined based on the state of bed and head joints (open or closed).

In the present study, bauxite-based refractory ceramic is considered as the base material of the bricks. At high temperature, the constitutive material is assumed to undergo small deformations (i.e. the displacement gradients are small, each component is small as compared to unity, $|u_{i,j}| << 1$) and to exhibit an isotropic linear elasticity as well as an isotropic steady state rate-dependent plasticity (secondary creep). Under these assumptions, the total strain second order tensor ($\overline{\overline{\varepsilon}}^{\,t}$) can be described by the symmetric part of the displacement vector ($\overline{u}$) with respect to the position vector ($\overline{X}$) of the material point according to:

$$\overline{\overline{\varepsilon}}^{\,t} = \frac{1}{2}\left(\frac{\partial \overline{u}}{\partial \overline{X}} + \left(\frac{\partial \overline{u}}{\partial \overline{X}}\right)^{\mathrm{T}}\right) \tag{1}$$

The total strain tensor can be additively decomposed into elastic ($\overline{\overline{\varepsilon}}^{\,\mathrm{e}}$) and viscoplastic ($\overline{\overline{\varepsilon}}^{\,\mathrm{vp}}$) second order strain tensors according to:

$$\overline{\overline{\varepsilon}}^{\,\mathrm{t}} = \overline{\overline{\varepsilon}}^{\,\mathrm{e}} + \overline{\overline{\varepsilon}}^{\,\mathrm{vp}} \tag{2}$$

The second order linear elastic strain tensor can be determined using Hooke's law for isotropic linear elasticity according to:

$$\overline{\overline{\varepsilon}}^{\,\mathrm{e}} = \frac{1+\nu}{Y}\,\overline{\overline{\sigma}} - \frac{\nu}{Y} tr(\overline{\overline{\sigma}})\overline{\overline{I}} \tag{3}$$

where, ν is the Poisson's ratio of the bulk material of the bricks and Y is the Young's modulus of the bulk material of the bricks. $\overline{\overline{\sigma}}$ and $\overline{\overline{I}}$ refer respectively to the second order local stress tensor and the second order identity tensor.

The steady state isotropic viscoplastic strain rate second order tensor ($\dot{\overline{\overline{\varepsilon}}}^{\mathrm{vp}}$) is expressed as [34]:

$$\dot{\overline{\overline{\varepsilon}}}^{\mathrm{vp}} = \frac{3}{2} A \ (\sigma_{eq})^{n-1} \ \overline{\overline{\sigma}}_d \tag{4}$$

where $A,\ n$ are the creep parameters of the bulk material of the bricks. σ_{eq} and $\overline{\overline{\sigma}}_d$ denote the Von Mises equivalent stress and the second order deviatoric stress tensor, respectively.

The deviatoric stress tensor and Von Mises equivalent stress are expressed as:

$$\overline{\overline{\sigma}}_d = \overline{\overline{\sigma}} - \left(\frac{1}{3}\right) tr(\overline{\overline{\sigma}})\overline{\overline{I}} \tag{5}$$

$$\sigma_{eq} = \sqrt{\left(\frac{3}{2}\right) \ \overline{\overline{\sigma}}_{\mathrm{d}} : \overline{\overline{\sigma}}_{\mathrm{d}}} \tag{6}$$

The required material parameters are taken from [35] and reported in table 1. For the sake of simplicity, no strain hardening of the constitutive material of the bricks is considered. In addition, symmetric creep behaviour is assumed (i.e. creep parameters in tension and compression are equal). Further details on the nonlinear homogenization analysis and the identification of the homogenized elastic viscoplastic behaviour of the four patterns and the transition criteria from one joint pattern to another are described in sections 3 and 4.

Table 1: Material parameters of bauxite refractory at T = 1000 °C [35].

Property	Value
Young's modulus (Y, MPa)	11000
Poisson's ratio (ν)	0.2
Creep stress exponent (n)	2.8
Creep power law multiplier (A, $s^{-1}\ MPa^{-\mathrm{n}}$)	2.77×10^{-8}

3 Periodic nonlinear homogenization of mortarless masonry structures

3.1 Joint pattern C

As indicated previously in the case of joint pattern C, head and bed joints are closed (see figure 2). Previous experimental studies show that when joints are closed, the mechanical behaviour of the masonry is similar to the mechanical behaviour of the base material of the bricks. Thus, the macroscopic elastic-viscoplastic behaviour of pattern C is isotropic, similar to that of the base material of the bricks and can be described by equations 1 - 6.

3.2 Joint pattern B

3.2.1 Micro modelling

In the case of pattern B, head joints are open, and bed joints are closed (see figure 2). The existence of open joints in the masonry results in a reduction in their effective stiffness [14, 15, 36, 37]. Thus, the macroscopic elastic-viscoplastic behaviour of pattern B is different from that of the base material of the bricks. For the purpose of studying the homogenized mechanical behaviour of periodic structures, like pattern B, and computing the effective elastic viscoplastic parameters, the finite element (FE) -based homogenization technique can be adopted [38–41].

To carry out homogenization of joint pattern B using FE technique, a periodic unit cell (UC) with volume (V_{UC}) has been selected from the periodic structure as illustrated in figure 3. Then, $3D-$FE simulations have been performed on the UC to characterise its homogenized elastic viscoplastic response. To account for the periodicity of the structure,

periodic boundary conditions have been applied to the UC's boundaries [42–44]. In contrast to homogeneous boundary conditions, periodic boundary conditions satisfy both boundary displacement periodicity and boundary traction periodicity. Moreover, homogeneous boundary conditions are over constrained conditions, violate stress periodicity of the boundaries and, therefore, are not recommended to be used for periodic UC subjected to shear loading conditions [42, 43].

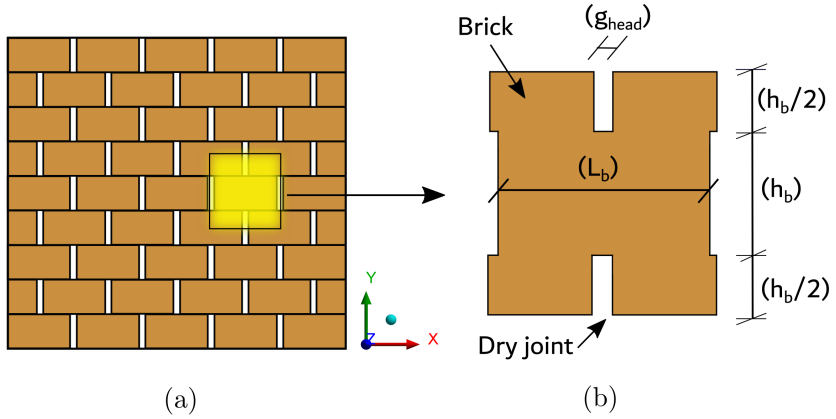

Figure 3: (a) Schematic of periodic mortarless masonry structure in pattern B. (b) Periodic unit cell selected from the structure and used for the nonlinear finite element based homogenization analysis.

Several FE numerical experiments of uniaxial tensile tests along the x, y and z directions and simple shear tests in the xy, xz, and yz planes (see figure 4) have been performed. The numerical models have been developed using ABAQUS software and the UC has been meshed with 3D quadrilateral elements with 1 mm size. For all cases, the UC has been subjected to an average or macroscopic stress (shear or normal) of 1.5 MPa. The base material of the bricks is considered to exhibit an isotropic linear elasticity, an isotropic steady state rate-dependent plasticity (secondary creep) and to obey the elastic and viscoplastic constitutive equations given in section 2.

To characterise the homogenized elastic behaviour of the UC and to avoid the contribution of the viscoplastic strain when calculating the effective elastic stiffness of the structure, first, purely elastic numerical simulations have been carried out. Then, viscoplastic numerical analysis have been performed on the UC to characterise its homogenized viscoplastic response. From figure 4, it can be seen that the periodicity of boundary displacements and

stresses are satisfied due to the applied periodic boundary conditions. From the uniaxial tensile and simple shear numerical tests of the UC subjected to macroscopic normal or shear stress of 1.5 MPa, the macroscopic strain tensor and the effective material parameters can be found.

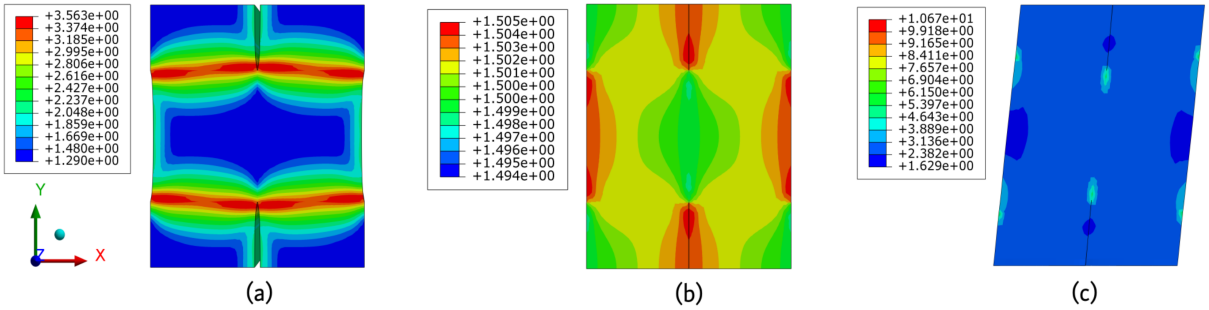

Figure 4: Von Mises stress (in MPa) distribution in a periodic unit cell subjected to periodic boundary conditions and (a) uniaxial tension along the x-direction (σ_{xx}=1.5 MPa), (b) uniaxial tension along the y-direction (σ_{yy}=1.5 MPa) and (c) simple shear in the xy plane (τ_{xy}=1.5 MPa).

3.2.2 Macroscopic constitutive equations

Macroscopic elastic behaviour

The first goal is to define a relation between macroscopic stress tensor and macroscopic elastic strain tensor (i.e. determine the effective elastic stiffness tensor of pattern B). Due to the existence of open joints, the macroscopic elastic behaviour of pattern B is orthotropic and can be described using equation 7. In the case of orthotropic linear elastic materials, the macroscopic stress tensor is related to the macroscopic elastic strain tensor through the macroscopic form of Hooke's law as following [45]:

$$\overline{\overline{\Sigma}} = \overline{\overline{\overline{\overline{C}}}}^{\,e} : \overline{\overline{E}}^{\,e} \tag{7}$$

where $\overline{\overline{\Sigma}}$ and $\overline{\overline{E}}^{\,e}$ are the second order macroscopic stress and elastic strain tensors while, $\overline{\overline{\overline{\overline{C}}}}^{\,e}$ is the fourth order macroscopic elastic stiffness tensor.

In equation 7, the second and fourth order tensors are symmetric and, therefore, they can be respectively reduced to 6×1 and 6×6 matrices using the Voigt notations [41]. The effective elastic fourth order tensor is characterized by 9 nonzero components and can be written in a matrix form, with respect to the principal material coordinate system,

using Voigt notations as follows [45]:

$$\overline{\overline{\overline{\overline{C}}}}^{\,\mathrm{e}} = \begin{bmatrix} \frac{1-\widetilde{\nu}_{23}\widetilde{\nu}_{32}}{\widetilde{E}_{22}\widetilde{E}_{33}\triangle} & \frac{\widetilde{\nu}_{21}+\widetilde{\nu}_{31}\widetilde{\nu}_{23}}{\widetilde{E}_{22}\widetilde{E}_{33}\triangle} & \frac{\widetilde{\nu}_{31}+\widetilde{\nu}_{21}\widetilde{\nu}_{32}}{\widetilde{E}_{22}\widetilde{E}_{33}\triangle} & 0 & 0 & 0 \\ \frac{\widetilde{\nu}_{12}+\widetilde{\nu}_{13}\widetilde{\nu}_{32}}{\widetilde{E}_{11}\widetilde{E}_{33}\triangle} & \frac{1-\widetilde{\nu}_{31}\widetilde{\nu}_{13}}{\widetilde{E}_{11}\widetilde{E}_{33}\triangle} & \frac{\widetilde{\nu}_{32}+\widetilde{\nu}_{31}\widetilde{\nu}_{12}}{\widetilde{E}_{11}\widetilde{E}_{33}\triangle} & 0 & 0 & 0 \\ \frac{\widetilde{\nu}_{13}+\widetilde{\nu}_{12}\widetilde{\nu}_{23}}{\widetilde{E}_{11}\widetilde{E}_{22}\triangle} & \frac{\widetilde{\nu}_{23}+\widetilde{\nu}_{13}\widetilde{\nu}_{21}}{\widetilde{E}_{11}\widetilde{E}_{22}\triangle} & \frac{1-\widetilde{\nu}_{12}\widetilde{\nu}_{21}}{\widetilde{E}_{11}\widetilde{E}_{22}\triangle} & 0 & 0 & 0 \\ 0 & 0 & 0 & \widetilde{G}_{12} & 0 & 0 \\ 0 & 0 & 0 & 0 & \widetilde{G}_{13} & 0 \\ 0 & 0 & 0 & 0 & 0 & \widetilde{G}_{23} \end{bmatrix} [MPa], \tag{8}$$

with,

$$\triangle = \frac{1 - \widetilde{\nu}_{12}\widetilde{\nu}_{21} - \widetilde{\nu}_{23}\widetilde{\nu}_{32} - \widetilde{\nu}_{31}\widetilde{\nu}_{13} - 2\widetilde{\nu}_{12}\widetilde{\nu}_{23}\widetilde{\nu}_{31}}{\widetilde{E}_{11}\widetilde{E}_{22}\widetilde{E}_{33}} \tag{9}$$

In the above equations, $\widetilde{E}$ and $\widetilde{\nu}$ denote respectively the macroscopic or effective Young's modulus and the macroscopic or effective Poisson's ratio. $\widetilde{G}$ is the macroscopic or effective shear modulus.

According to the average theorems, when a uniform stress is applied to the boundary surfaces of the UC, the macroscopic stress is equal to the applied stress (i.e. $\overline{\overline{\sigma}} = \overline{\overline{\Sigma}}$) [41]. Another possible approach for calculating the macroscopic stress is to integrate the local stress fields over the volume of the UC (V_{UC}) according to Hill's definition as follows [38, 46, 47]:

$$\overline{\overline{\Sigma}} = \langle \overline{\overline{\sigma}} \rangle = \frac{1}{V_{\mathrm{UC}}} \int_{V_{\mathrm{UC}}} \overline{\overline{\sigma}} dV \tag{10}$$

From the simulated combination of uniaxial tensile and simple shear tests, the local strains can be obtained from solving the boundary value problem of the UC subjected to average normal or shear stress of 1.5 MPa. From the local elastic strains, the macroscopic elastic strains can be calculated. Then, using equations 7 - 9, the 9 nonzero components of $\overline{\overline{\overline{\overline{C}}}}^{\,\mathrm{e}}$ can be found and the relation between the macroscopic stress tensor and macroscopic elastic strain tensor can be established.

In previous studies, two main approaches have been used to calculate the macroscopic strain fields [38, 46, 48–52]. The first approach is based on calculating the macroscopic total strain by integrating the local total strain ($\overline{\overline{\varepsilon}}^{\,t}$) over the volume of the UC according

to [38, 48–50]:

$$\overline{\overline{E}}^{\,t} = \langle \overline{\overline{\varepsilon}}^{\,t} \rangle = \frac{1}{V_{\mathrm{UC}}} \int_{V_{\mathrm{UC}}} \overline{\overline{\varepsilon}} dV \tag{11}$$

In the second approach, the macroscopic elastic strains are calculated from the average change in the displacements of the UC's corners (i.e. by dividing the change in displacements of the corners by the initial dimensions of the UC) [46, 51, 52]. If there are neither gaps nor cracks in the UC, both techniques converge to the same value. However, in the case of joint pattern B, the macroscopic elastic strains cannot be computed by integrating the micro (or local) strains over the volume of the UC (first approach). As, the presence of open joints within the UC leads to discontinuous displacement fields (see figure 5), because there is neither viscosity nor rigidity in the volume of the gaps (i.e. local strains within the gaps are unknown) [38, 46]. Therefore, in the present study, the second approach has been used to calculate the macroscopic strains. The calculated 9 nonzero components of $\overline{\overline{\overline{\overline{C}}}}^{\,e}$ are reported in table 2. Now, the relationship between macroscopic stresses and macroscopic elastic strains is established. Further details on defining the macroscopic viscoplastic behaviour law are given below.

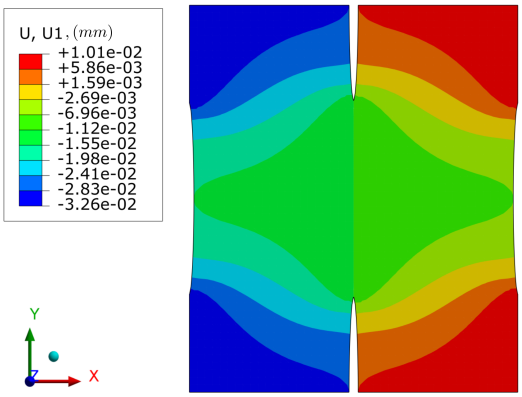

Figure 5: Displacement discontinuity in a periodic unit cell subjected to uniaxial tension along the x direction. The displacement discontinuity is caused by the presence of open head joints (vertical gaps).

Macroscopic viscoplastic behavior

The second goal is to define a macroscopic constitutive law to describe the viscoplastic behaviour of joint pattern B. Time variations of the macroscopic total strains (instantaneous elastic and viscoplastic) in a periodic UC subjected to uniaxial and simple shear constant

stress loading conditions ($\sigma_{ii} = \tau_{ij} = 1.5$ MPa) are shown in figure 6. It can be seen that the macroscopic elastic viscoplastic behaviour of joint pattern B is orthotropic (due to the presence of joints) and the homogenized mechanical responses of the material in the y and z directions are similar (as there are no joints in the z direction, and joints in the y direction are closed). In order to describe the macroscopic viscoplastic behaviour of joint pattern B, an orthotropic creep equation is required. It should be noted that equation 4 is suitable only for describing the local creep behaviour of isotropic materials such as joint pattern C.

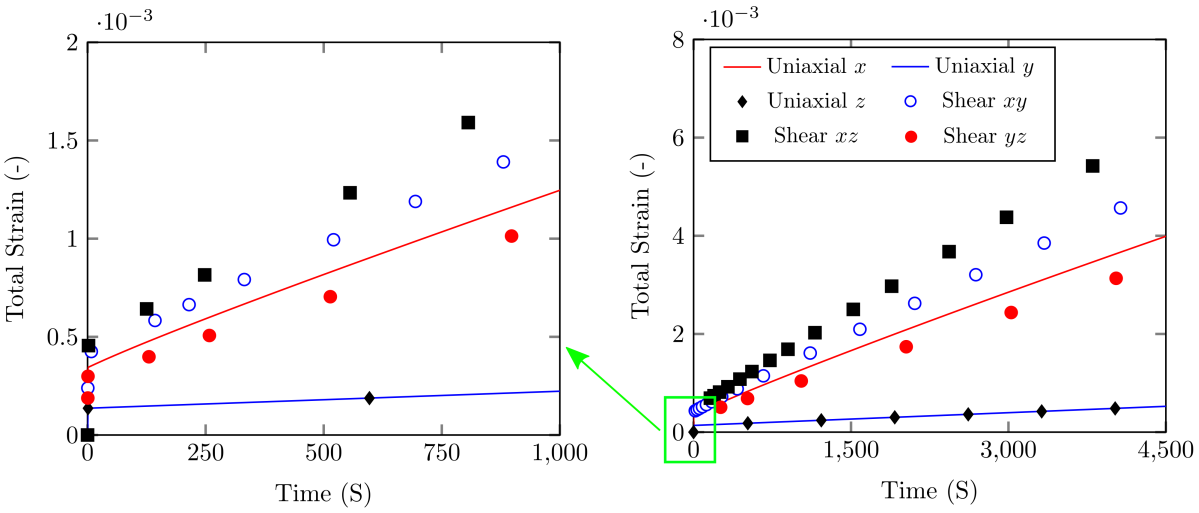

Figure 6: Macroscopic total strains in a periodic unit cell subjected to periodic boundary conditions as well as constant stress uniaxial tension (in the x, y and z directions) and simple shear loading (in the xy, xz and yz planes) ($\Sigma_{\text{ii}} = \Sigma_{\text{ij}}$=1.5 MPa). The macroscopic elastic viscoplastic behaviour of the structure is orthotropic.

The orthotropic homogenized steady-state viscoplastic behaviour of heterogeneous solids can be described using the macroscopic form of equation 4 developed by Tsuda et al. [38, 39, 52, 53]. The main advantage of this constitutive law is that using the same parameters of the base material, the orthotropic homogenized viscoplastic behaviour of heterogeneous solids can be found. The constitutive law is obtained through averaging the local fields (σ, $\overline{\overline{\dot{\varepsilon}}}^{\,\text{vp}}$, σ_{eq}) over the volume of the UC and using a localization tensor according to:

$$\overline{\overline{\dot{E}}}^{\,vp} = \frac{1}{2} A \left(\Sigma_{eq}\right)^{n-1} \overline{\overline{\overline{\overline{N}}}} : \overline{\overline{\Sigma}} \tag{12}$$

with A and n are materials parameters of the bricks, reported in table 1, Σ_{eq} and $\overline{\overline{\overline{\overline{N}}}}$ are

the macroscopic equivalent stress and a fourth order tensor with the same meaning of the localization tensor. The $\overline{\overline{\overline{\overline{N}}}}$ tensor accounts for the orthotropy and compressibility (in the x direction, see figure 6) of the structure and enables using the creep parameters of the constitutive material (i.e. bridge between the micro and macro scales). The $\overline{\overline{\overline{\overline{N}}}}$ tensor is symmetric and can be represented by 6×6 matrix using the Voigt notations. $\overline{\overline{\overline{\overline{N}}}}$ is characterized by 9 nonzero components and can be represented, with respect to the principal material coordinate system, as:

$$\overline{\overline{\overline{\overline{N}}}} = \begin{bmatrix} N_{11} & N_{12} & N_{13} & 0 & 0 & 0 \\ N_{12} & N_{22} & N_{23} & 0 & 0 & 0 \\ N_{13} & N_{23} & N_{33} & 0 & 0 & 0 \\ 0 & 0 & 0 & N_{44} & 0 & 0 \\ 0 & 0 & 0 & 0 & N_{55} & 0 \\ 0 & 0 & 0 & 0 & 0 & N_{66} \end{bmatrix} \tag{13}$$

For heterogeneous solids, the macroscopic equivalent stress is written in terms of the macroscopic stress tensor and $\overline{\overline{\overline{\overline{N}}}}$ as [38, 52, 54]:

$$\Sigma_{eq} = \sqrt{\frac{1}{2}\left(\overline{\overline{\Sigma}}\right)^{T} : \overline{\overline{\overline{\overline{N}}}} : \overline{\overline{\Sigma}}} \tag{14}$$

Here $\left(\overline{\overline{\Sigma}}\right)^{T}$ is the transpose of the macroscopic stress second order tensor. The macroscopic equivalent viscoplastic strain rate ($\dot{E}^{vp}_{eq}$) is defined in terms of $\overline{\overline{\overline{\overline{N}}}}$ and $\dot{\overline{\overline{E}}}^{\,vp}$ as follows [38]:

$$\dot{E}^{vp}_{eq} = \sqrt{2\left(\dot{\overline{\overline{E}}}^{\,vp}\right)^{T} : \left(\overline{\overline{\overline{\overline{N}}}}\right)^{-1} : \dot{\overline{\overline{E}}}^{\,vp}} \tag{15}$$

By combining equations 12 - 14 and using the combinations of uniaxial and simple shear finite element numerical tests presented before, the 9 non-zero components of the tensor $\overline{\overline{\overline{\overline{N}}}}$ can be calculated and the macroscopic creep law can be defined.

Under uniaxial loading and periodic boundary conditions the shear components of the macroscopic stress tensor vanish. Therefore, the first 6 components of $\overline{\overline{\overline{\overline{N}}}}$ can be defined as follows [38]:

- Uniaxial tension along the x-direction

$$N_{11} = 2\left(\frac{1}{\Sigma_{xx}}\right)^2 \left(\frac{\Sigma_{xx}\dot{E}^{vp}_{xx}}{A}\right)^{\frac{2}{n+1}} \tag{16}$$

$$N_{12} = \left(\frac{\dot{E}^{vp}_{yy}}{\dot{E}^{vp}_{xx}}\right) N_{11} \tag{17}$$

$$N_{13} = \left(\frac{\dot{E}^{vp}_{zz}}{\dot{E}^{vp}_{xx}}\right) N_{11} \tag{18}$$

- Uniaxial tension along the y-direction:

$$N_{22} = 2\left(\frac{1}{\Sigma_{yy}}\right)^2 \left(\frac{\Sigma_{yy}\dot{E}^{vp}_{yy}}{A}\right)^{\frac{2}{n+1}} \tag{19}$$

$$N_{12} = \left(\frac{\dot{E}^{vp}_{xx}}{\dot{E}^{vp}_{yy}}\right) N_{22} \tag{20}$$

$$N_{23} = \left(\frac{\dot{E}^{vp}_{zz}}{\dot{E}^{vp}_{yy}}\right) N_{22} \tag{21}$$

- Uniaxial tension along the z-direction:

$$N_{33} = 2\left(\frac{1}{\Sigma_{zz}}\right)^2 \left(\frac{\Sigma_{zz}\dot{E}^{vp}_{zz}}{A}\right)^{\frac{2}{n+1}} \tag{22}$$

$$N_{13} = \left(\frac{\dot{E}^{vp}_{xx}}{\dot{E}^{vp}_{zz}}\right) N_{33} \tag{23}$$

$$N_{23} = \left(\frac{\dot{E}^{vp}_{yy}}{\dot{E}^{vp}_{zz}}\right) N_{33} \tag{24}$$

Under shear loading and periodic boundary conditions, the normal components of $\overline{\overline{\Sigma}}$ vanish and the shear components of $\overline{\overline{\overline{N}}}$ are written as follows:

- Simple shear in the xy-plane:

$$N_{44} = 2\left(\frac{1}{\Sigma_{xy}}\right)^2 \left(\frac{\Sigma_{xy}\dot{E}^{vp}_{xy}}{A}\right)^{\frac{2}{n+1}} \tag{25}$$

- Simple shear in the xz-plane:

$$N_{55} = \left(\frac{1}{\Sigma_{xz}}\right)^2 \left(\frac{\Sigma_{xz}\dot{E}^{vp}_{xz}}{A}\right)^{\frac{2}{n+1}} \tag{26}$$

- Simple shear in the yz-plane:

$$N_{66} = 2\left(\frac{1}{\Sigma_{yz}}\right)^2 \left(\frac{\Sigma_{yz}\dot{E}^{vp}_{yz}}{A}\right)^{\frac{2}{n+1}} \tag{27}$$

In the previous equations, the values of macroscopic normal and shear stresses are equal to the applied average stresses. The macroscopic viscoplastic strain rates are determined from the time derivative of the macroscopic viscoplastic strain ($\overline{\overline{E}}^{\,\mathrm{vp}}$ calculated from the displacement of the corners of the UC as described before). The obtained values of the 9 none-zero components of $\overline{\overline{\overline{\overline{N}}}}$ are reported in table 2. It can be observed that the y and z components of the tensor are almost the same (due to the absence of joints in the z direction, only one brick in the depth of the wall, and the absence of open joints in the y direction). To compare the components of the $\overline{\overline{\overline{\overline{N}}}}$ tensor of joint pattern B and those of the constitutive material, the components of $\overline{\overline{\overline{\overline{N}}}}$ tensor have been identified for joint pattern C, using the same approach, and reported in table 2. It can be seen that, in the case of pattern B, the y and z components of $\overline{\overline{\overline{\overline{N}}}}$ tensor are almost equal to those of the constitutive material of the bricks.

3.3 Joint pattern O

As presented earlier, in the case of pattern O, both head and bed joints are open. It can be seen from figure 2 that the masonry structure is composed of an array of separated bricks and the masonry structure is disconnected. For the purpose of computing the effective mechanical parameters of the structure (elastic and viscoplastic), one cannot use finite element-based homogenization approach (micro modelling) presented earlier because the boundary value problem of the UC is not clearly defined. However, the mechanical parameters of the constitutive material can be used to define the effective mechanical properties of joint pattern O [14, 15, 36]. Due to the existence of open joints in the x and y directions, the effective elastic and viscoplastic mechanical parameters of the masonry

structure in the x and y directions are very small. Therefore, the effective Young's modulus and the components of $\overline{\overline{\overline{N}}}$ in directions x and y are zero ($\widetilde{E}_{\mathrm{x}} = \widetilde{E}_{\mathrm{y}} = 0$, see the coordinate system in figure 3). In addition, the effective Young's modulus and $\overline{\overline{\overline{N}}}$ components in z direction are equal to those of the constitutive material due to the absence of joints in the z direction (only one brick in the z direction). The $\overline{\overline{\overline{C}}}^{\,\mathrm{e}}$ and $\overline{\overline{\overline{N}}}$ tensors of joint pattern O are reported in table 2. To facilitate the numerical computations and to avoid numerical singularities and solution divergence, a very small value has been assigned to $\widetilde{E}_{\mathrm{x}}$, $\widetilde{E}_{\mathrm{y}}$, $\widetilde{\nu}_{\mathrm{xy}}$, $\widetilde{\nu}_{\mathrm{xz}}$, $\widetilde{\nu}_{\mathrm{yz}}$ and $\widetilde{G}_{\mathrm{xy}}$ instead of zero.

3.4 Joint pattern H

In the case of joint pattern H, head joints are closed whereas bed joints are open (see figure 2). The masonry structure is composed of an array of separated courses of bricks (in the y-direction). Thus, the structure has zero macroscopic stiffness in the y-direction (due to the presence of open joints) while it has stiffness in the x (as all joints are closed in this direction) and z-directions (only one brick in the z direction) [14, 15, 36]. Similar to pattern O, one cannot use finite element-based homogenization approach presented earlier because the boundary value problem of the UC is not clearly defined. However, the mechanical parameters of the constitutive material can be used to define the effective mechanical properties of joint pattern H. Since bed joints are open, the macroscopic stiffness of the structure in direction y is very small and $\widetilde{E}_{\mathrm{y}}$ is zero. Thus, the components of $\overline{\overline{\overline{N}}}$ in the y direction are also equal to zero. However, the effective Young's modulus and $\overline{\overline{\overline{N}}}$ components in x and z directions are equal to those of the constitutive material due to the absence of joints in the z direction and the absence of open joints in x direction. The $\overline{\overline{\overline{C}}}^{\,\mathrm{e}}$ and $\overline{\overline{\overline{N}}}$ tensors of joint pattern H are reported in table 2.

Table 2: Effective elastic and viscoplastic 4th order tensors of the four joint patterns.

Pattern	$\overline{\overline{\overline{\overline{C}}}}$ (MPa)						$\overline{\overline{\overline{\overline{N}}}}$ (-)					
	1	0	0	0	0	0	0	0	0	0	0	0
		1	0	0	0	0		0	0	0	0	0
O			11000	0	0	0			2.01	0	0	0
				0	0	0				0	0	0
		sym.			4583	0		*sym.*			6.01	0
						4583						6.01
	11485	0	2291	0	0	0	2.01	0	−0.99	0	0	0
		1	0	0	0	0		0	0	0	0	0
H			11485	0	0	0			2.01	0	0	0
				0	0	0				0	0	0
		sym.			4583	0		*sym.*			6.01	0
						4583						6.01
	4430	1113	1103	0	0	0	6.25	−1.10	−0.49	0	0	0
		11738	2560	0	0	0		2.01	−0.99	0	0	0
B			11733	0	0	0			1.99	0	0	0
				3602	0	0				7.18	0	0
		sym.			3315	0		*sym.*			8.25	0
						4583						6.01
	12222	3055	3055	0	0	0	2.01	−0.99	−0.99	0	0	0
		12222	3055	0	0	0		2.01	−0.99	0	0	0
C			12222	0	0	0			2.01	0	0	0
				4583	0	0				6.01	0	0
		sym.			4583	0		*sym.*			6.01	0
						4583						6.01

4 Joints closure and reopening criteria

As discussed above, each joint pattern has different homogeneous elastic viscoplastic response. In normal operating conditions, the masonry is subjected to cyclic thermal or mechanical loading and unloading. Thus, head or bed or both joints may close and reopen. Consequently, the masonry structure changes from one joint pattern to another leading to a change in the macroscopic elastic viscoplastic behaviour of the structure. In the present work, this change has been taken into account by using suitable joints closure, reopening and pattern transition criteria.

Before loading, head and bed joints are open and the masonry structure can be fully described by pattern O. Under compression loads, the thickness of head or bed or both joints decreases gradually from the initial value (g_0, around 0.1 to 0.2 mm) to zero and the structure changes from pattern O to either pattern H (when head joints close) or

pattern B (when bed joints close). In addition, the structure may change from pattern O to pattern C if both head and bed joints close. Based on the instantaneous thickness of the joints g, head and bed joints are considered to be open as:

$$Joint\ open \qquad if \qquad g_{\text{bed or head}} > 0 \tag{28}$$

As the equivalent material properties of the masonry are piecewise constant, the displacement increment at every point in the structure linearly depends on the increment in the macroscopic quantities [14, 15]. Thus, the instantaneous thickness of the head and bed joints can be written in terms of the macroscopic components of total strains in the x (E^{t}_{xx}) and y (E^{t}_{yy}) directions as:

$$g_{\text{head}} = g_{0,\text{ head}} + M_{\text{x}} E^{\text{t}}_{\text{xx}} \tag{29}$$

$$g_{\text{bed}} = g_{0,\text{ bed}} + M_{\text{y}} E^{\text{t}}_{\text{yy}} \tag{30}$$

Where g_{bed} and g_{head} are the instantaneous thickness of bed and head joints, respectively. $g_{0,\text{bed}}$ and $g_{0,\text{head}}$ denote the initial thickness of bed and head joints, respectively. M_{y} and M_{x} are parameters with the same meaning of the localization tensor, and they depend on the dimensions of the brick ($M_{\text{y}} = h_{\text{b}}$ and $M_{\text{x}} = l_{\text{b}}$). E^{t}_{yy} and E^{t}_{xx} are the macroscopic total strains (elastic and viscoplastic strains) in the y and x directions.

With regard to joints reopening criterion, head and bed joints can reopen if the normal stress to the surface of the joint (head or bed) is higher than zero (i.e. tensile stress). In other words, a head joint can reopen if $\sigma_{\text{xx}} > 0$ and a bed joint can reopen if $\sigma_{\text{yy}} > 0$. As the macroscopic stresses are linearly dependent on local stresses (see equation 10), joints reopening criterion can be rewritten in terms of macroscopic stresses using localization tensor $\Sigma_{\text{yy}} \longrightarrow \sigma_{\text{yy}}$ and $\Sigma_{\text{xx}} \longrightarrow \sigma_{\text{xx}}$. The joints closure, reopening and transition criteria from joint pattern O to pattern H, joint pattern H to pattern B, joint pattern H to pattern C, joint pattern B to pattern C, and the opposite are presented in figure 7.

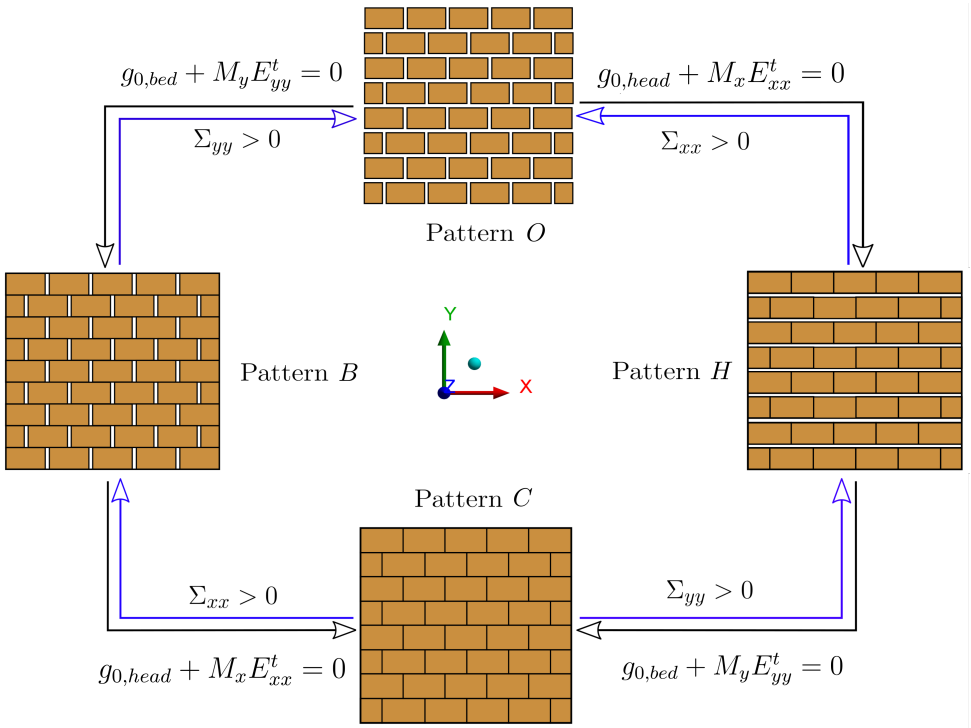

Figure 7: Schematics of all possible joint patterns of mortarless refractory masonry structure and joints closure and reopening criteria due to loading and unloading. Joints closure criteria are written in terms of macroscopic total strains. Joints reopening criteria are defined in terms of macroscopic stresses.

5 Results and discussion

5.1 Comparisons between the micro and macro modelling

The main aim of this section is to assess the accuracy of the developed macroscopic elastic viscoplastic numerical model. For this purpose, the equivalent material model (hereafter will be called macro model) has been implemented in the finite element code, Abaqus [55], with a user material subroutine UMAT. Then, it has been used to simulate uniaxial, simple shear and biaxial numerical experiments. Two different loading conditions have been considered namely, constant stress (creep) and constant strain loading (stress relaxation). For both loading conditions, comparisons between results from the macro and micro models are performed. In the case of macro modelling, the bricks and the joints are replaced by an equivalent homogeneous medium and the macro constitutive laws (equations 7 - 27) are used. Whereas, in the case of micro modelling, the bricks and joints are considered and the micro constitutive laws (equations 1 - 6) are used.

For joint pattern B, comparisons between average total strains (elastic and viscoplastic strains) obtained from the micro and macro models for both constant stress uniaxial tensile load in the x, y and z directions and simple shear load with respect to the xy, xz and yz planes are shown in figure 8. The comparisons are presented for three constant stress levels in the respective direction. Good agreements between the results obtained from the macro and micro models can be observed. In addition, it can be observed that the macroscopic elastic viscoplastic behaviour of pattern B is orthotropic due to the presence of open joints. In the case of uniaxial loading in the y and z directions, values of the macroscopic total strains ($E^{\mathrm{t}}_{\mathrm{yy}}$ and $E^{\mathrm{t}}_{\mathrm{zz}}$) are almost the same because there are neither open joints in the y direction nor in the z direction. However, $E^{\mathrm{t}}_{\mathrm{yy}}$ and $E^{\mathrm{t}}_{\mathrm{zz}}$ are less than $E^{\mathrm{t}}_{\mathrm{xx}}$, because the presence of open joints in the x direction leads to a decrease in the effective stiffness of the structure and compressibility in the respective direction.

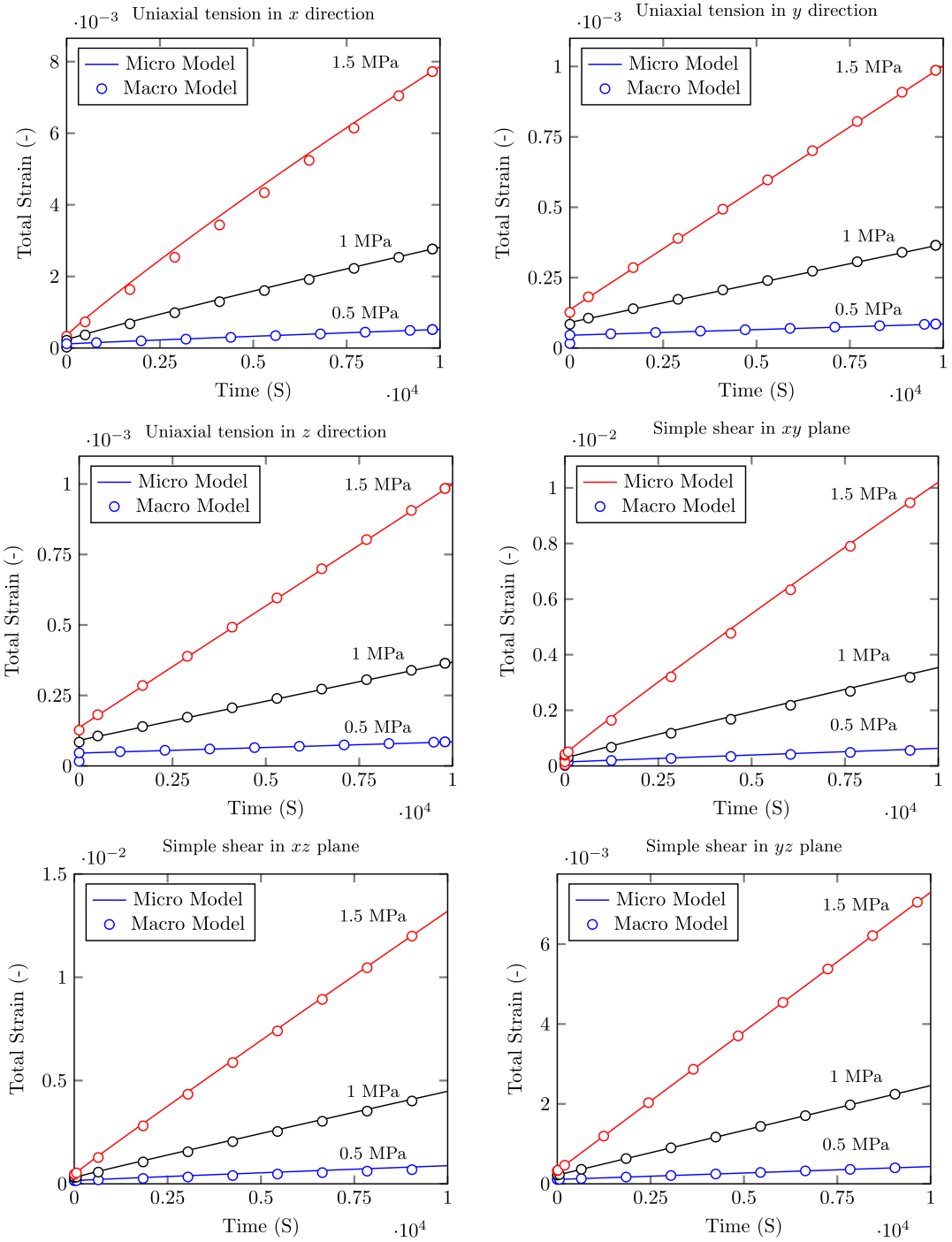

Figure 8: Comparisons between average total strains obtained from the detailed micro model (bricks and joints are considered) and macro model (bricks and joints are replaced by equivalent homogeneous medium) for constant stress uniaxial tension (in the x, y and z directions) and simple shear loadings (in the xy, xz and yz planes).

It should be noted that the previous constant stress loading conditions (uniaxial and simple shear) are used to identify the elastic viscoplastic parameters of the structure and, therefore, the agreements between the micro and macro models results are predicted. To

further examine the macro model and the identification technique, comparisons between the results of the micro and macro model under two different loading conditions (from those used in the identification) are carried out. The two loading conditions are biaxial constant stress loading and constant strain rate uniaxial loading. In the biaxial constant stress loading case, the following combination of compressive and tensile stresses are considered: compressive stress of 3 MPa in the x direction and tensile stress of 1 MPa in the y direction ($\Sigma_{xx} = -3\ MPa$ and $\Sigma_{yy} = 1\ MPa$). Comparisons between average total strains obtained from the micro and macro models are presented in figure 9. Good agreements between the micro and macro models are observed.

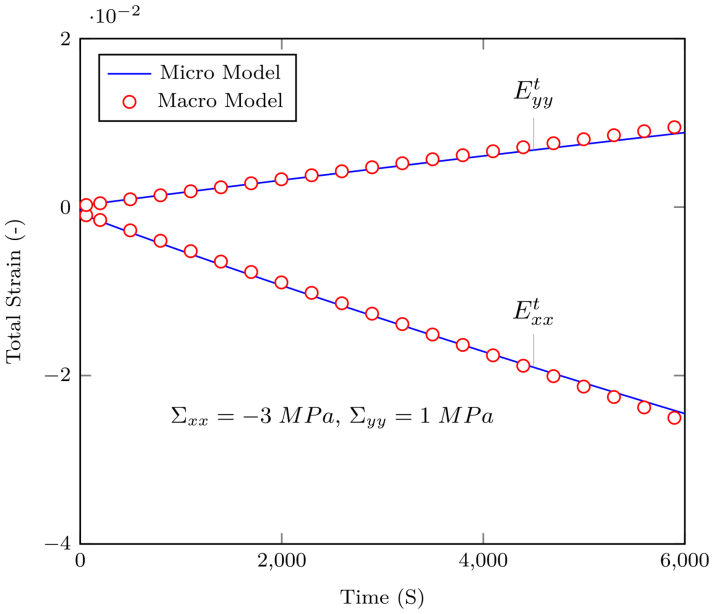

Figure 9: Comparisons between average total strains obtained from detailed micro model (bricks and joints are considered) and macro model (bricks and joints are replaced by equivalent homogeneous medium) for constant stress biaxial loading (compression in the x direction and tension in the y direction).

In the second loading case, comparisons between average stresses obtained from the micro and macro models for constant strain rate uniaxial tensile loading in the x, y and z directions and simple shear with respect to the xy, xz and yz planes are shown in figure 10. The comparisons are presented for three constant strain rate levels. Good agreements between the results obtained from the macro and micro models can be observed. Overall, the stresses increase sharply due to load application and then, during holding, there is a decay due to stress relaxation. Again, similar values of macroscopic stresses have been

observed in the case of uniaxial loading in the y and z directions. However, Σ_{yy} and Σ_{zz} are higher than Σ_{xx}, because the effective stiffness of the structure in the x direction is lower than that in the y and z directions.

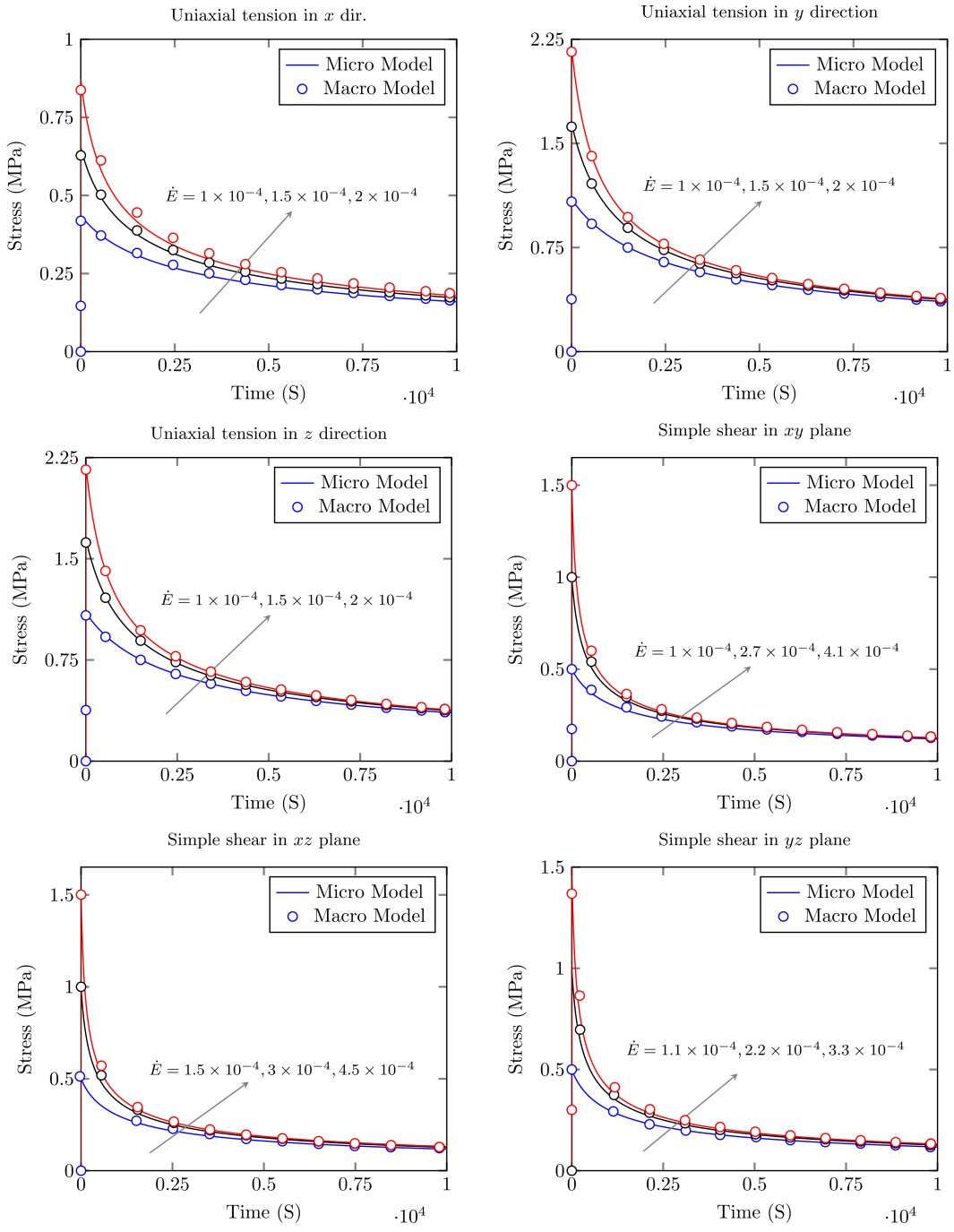

Figure 10: Comparisons between average macro stresses obtained from detailed micro model (bricks and joints are considered) and macro model (bricks and joints are replaced by equivalent homogeneous medium) for constant strain rate uniaxial tension (in the x, y and z directions) and simple shear loadings (in the xy, xz and yz planes).

5.2 Modelling of masonry structures subjected to different loading conditions

The previous results have shown the capability of the developed model to describe the orthotropic and rate-dependent homogenized behaviour of the four periodic joint patterns of mortarless masonry structure described before. The focus now is to model masonry structures subjected to different loading conditions and to take into account joints closure and reopening due to loading and unloading and their impact on the elastic viscoplastic behaviour of masonry structures.

In order to validate the present numerical models, comparative studies with experimental results reported in [14,56–58] of Magnesia Chromite refractory masonry walls subjected to biaxial compression load at room temperature and 1200 °C are carried out. The biaxial compression test setup is shown in figure 11. Magnesia Chromite bricks with length of 124 mm, height of 76 mm and depth of 185 mm are periodically arranged in a running bond texture. The mechanical parameters of the constitutive material of the bricks are reported in table 3. The size of the wall is $1100 \times 1100 \times 185\ mm^3$ and it is made up of 15 courses, all of them are active. The wall is surrounded by four ceramic plates, two of them are fixed while, the other two can move thanks to two hydraulic jacks.

For the purpose of measuring the displacement in the x (perpendicular to the contact surfaces of head joints) and y (perpendicular to the contact surfaces of bed joints) directions, four linear variable differential transformers (LVDT) are used (see Fig. 11).The testing procedures were as following: first a pre-compression load was applied to the two moving ceramic plates at the same time and then, it was stopped in the direction for which the LVDTs detected a displacement while continuing in the second direction until the LVDTs, in the corresponding direction, detected a displacement. Finally, monotonically increasing loads were applied to both directions at the same time. For the high temperature test, the test field was covered by a heating hood. The temperatures of the top face (hot face) and bottom face (cold face) were measured. During heating, the masonry wall was free to expand. Once the wall reached the thermal steady state, the compression loads were applied similar to the room temperature test. The temperatures of the hot and cold faces during load application were around 1200 °C and 800° C, respectively. Further details

about the experimental setup are reported in references [14, 56–58].

Table 3: Mechanical properties of Magnesia Chromite bricks at different temperatures [31, 56, 58, 59].

Temperature (°C)	Y (GPa)	ν (-)	n (-)	A ($S^{-1}MPa^{-n}$)
25	28.5	0.2	———	
800	15.4	0.2	———	
1000	10.6	0.2	———	
1100	9.8	0.2	2.86	1.18×10^{-16}
1200	9.1	0.2	2.86	2.77×10^{-16}

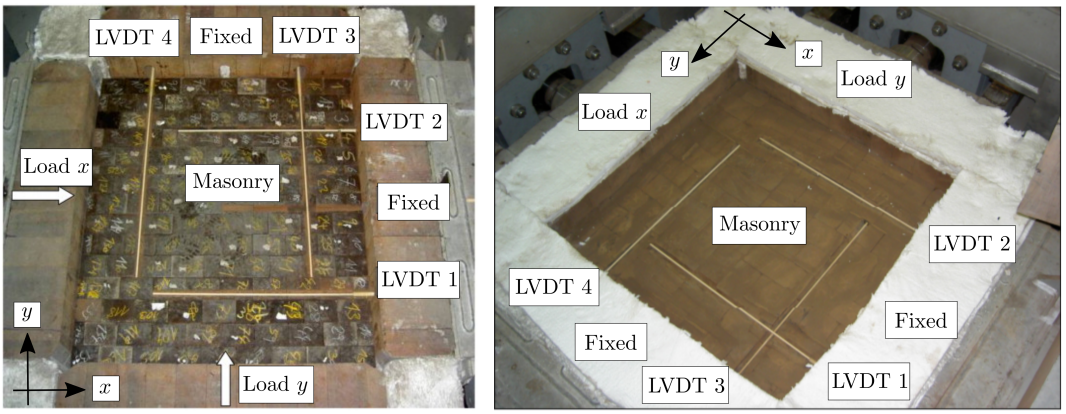

(a) (b)

Figure 11: Setup of the biaxial compression tests a) at room temperature and b) 1200 °C of Magnesia Chromite refractory masonry wall [14, 56–58].

The finite element models of the room and high temperature tests were developed using ABAQUS software and the wall was meshed with 3D quadrilateral elements. The four ceramic loading plates (fixed and moving) are replaced by rigid plates. The masonry (bricks and dry joints) is replaced by an equivalent material model whose mechanical properties depend on the state of bed and head joints (open or closed). The effective elastic and viscoplastic parameters of the four joint patterns are computed using FE based nonlinear homogenization technique, described in section 3.2, and are reported in tables A1 and A2 in the appendix. For room temperature test, the mechanical behavior of the masonry is assumed to be elastic while, for high temperature test it was assumed to be elastic-viscoplastic. In both cases, the macroscopic behavior changes with the change of joint pattern (i.e., closure of bed, head or both joints).

Comparisons between experimental and numerical stress-strain diagrams of masonry

walls subjected to biaxial compression at room temperature and 1200 °C are reported in figure 12. The strains, in the x and y directions, are calculated from the average displacements measured by the LVDTs and the stresses were determined from the resulting reaction forces of the two moving ceramic loading beams. It can be noticed that the present multi scale numerical model can reproduce, with reasonable accuracy, the mechanical behavior of the masonry structure under biaxial compression at either room temperature or 1200 °C. It can be noticed from figure 12 that the macroscopic mechanical behavior in both x and y directions is orthotropic. This can be attributed to that the number of joints in the x and y directions, the length and height of the bricks are different. Furthermore, the macroscopic behavior of the wall is nonlinear due to change of the macroscopic mechanical parameters of the masonry with the gradual closure of the joints. As compared to room temperature test, the strains (and displacements, see figures 13 and 14) in the x and y directions are higher. This can be attributed to that the decrease of the material stiffness at high temperature and viscoplasticity. Joint patterns by the end of load application step of the two tests are presented in figure 15. Higher percentage of closed bed and head joints are noticed in the case of the test at 1200 °C as compared to room temperature test.

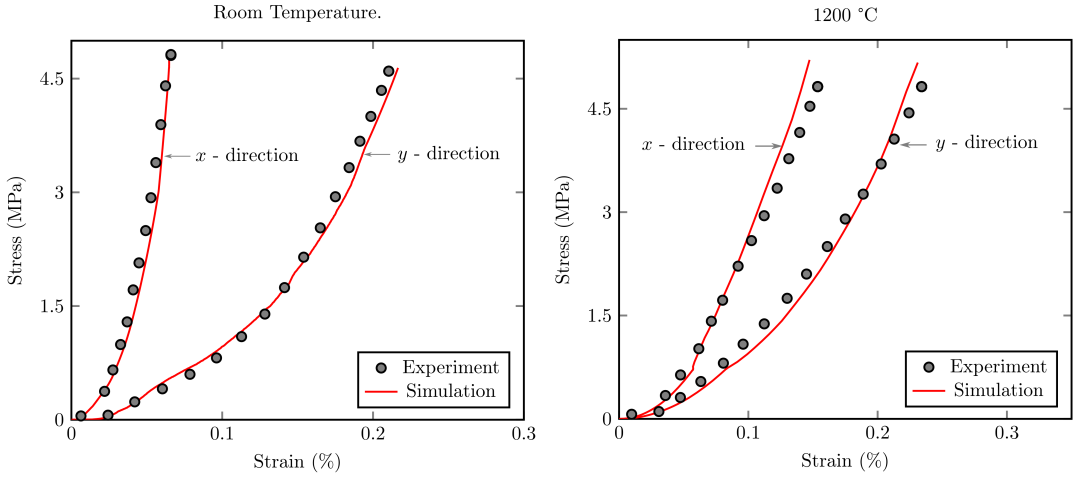

Figure 12: Stress-strain diagrams of refractory masonry wall subjected to biaxial compression load at a) room temperature and b) 1200 °C: experimental and numerical results.

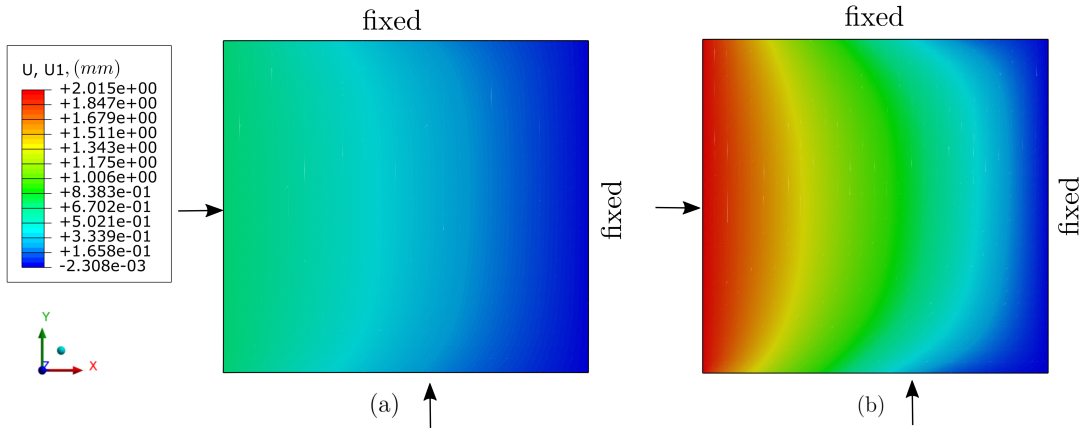

Figure 13: Horizontal displacement fields, in the x direction, in refractory masonry wall subjected to biaxial compression load at a) room temperature and b) 1200 °C. The word fixed indicates the location of the fixed rigid plates, while the arrows indicate the location and load direction of the moving rigid plates. The interactions between the contact surfaces of the wall and the fixed and moving rigid plates are considered using frictional contact.

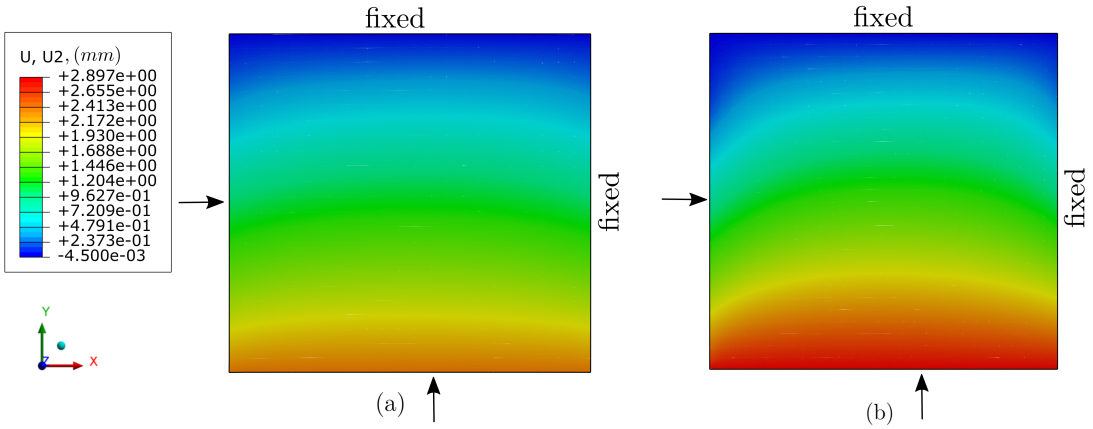

Figure 14: Vertical displacement fields, in the y direction, in refractory masonry wall subjected to biaxial compression load at a) room temperature and b) 1200 °C. The word fixed indicates the location of the fixed rigid plates, while the arrows indicate the location and load direction of the moving rigid plates. The interactions between the contact surfaces of the wall and the fixed and moving rigid plates are considered using frictional contact.

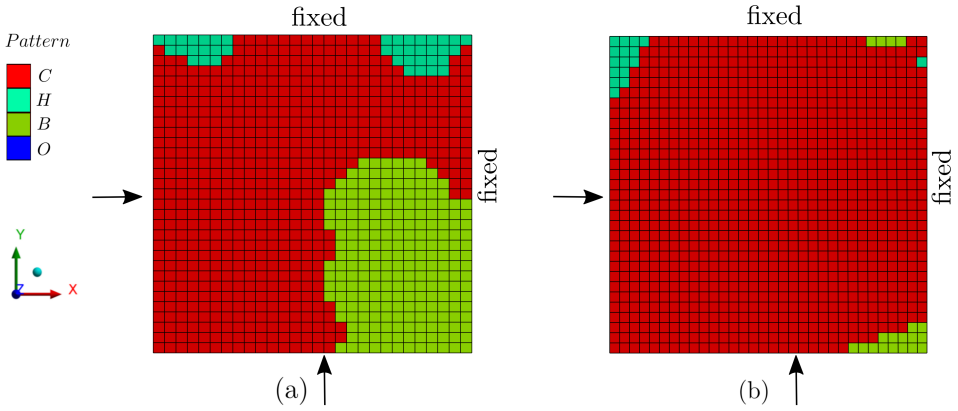

Figure 15: Joints pattern in a refractory masonry wall subjected to biaxial compression load at a) room temperature and b) 1200 °C. The word fixed indicates the location of the fixed rigid plates, while the arrows indicate the location and load direction of the moving rigid plates. The interactions between the contact surfaces of the wall and the fixed and moving rigid plates are considered using frictional contact.

Schematics of the masonry structure geometry subjected to uniaxial compression in x and y directions as well as the boundary conditions are presented in figure 16. Refractory bricks with length of 250 mm, height of 76 mm and depth of 185 mm are periodically arranged in a running bond texture. The base material of the bricks is Bauxite based refractories with material parameters reported in table 1. The size of the masonry structure is $1100 \times 1100 \times 185\ mm^3$ and it is made up of 14 courses. All the courses are active as the loads are applied to the simulated rigid plates, see figure 16. Friction forces between the rigid plates and the masonry and between the masonry and the ground are taken into account by considering friction contact between their adjacent surfaces (coefficient of friction = 0.5). The number of dry bed and head joints is 14 and 4 joints, respectively, with 0.1 mm thickness. The structure is assumed to be laid on the ground (xy- plane) and the gravity effects are considered. Two loading, holding and unloading (LHU) conditions are considered, to predict the creep and stress relaxation behaviour of the structure, namely constant displacement load and constant stress load. The loading, holding and unloading steps are as follows: displacement or stress load is applied (first step, loading), then kept constant for a specific time (second step, holding) and finally unloading (third step, load removal).

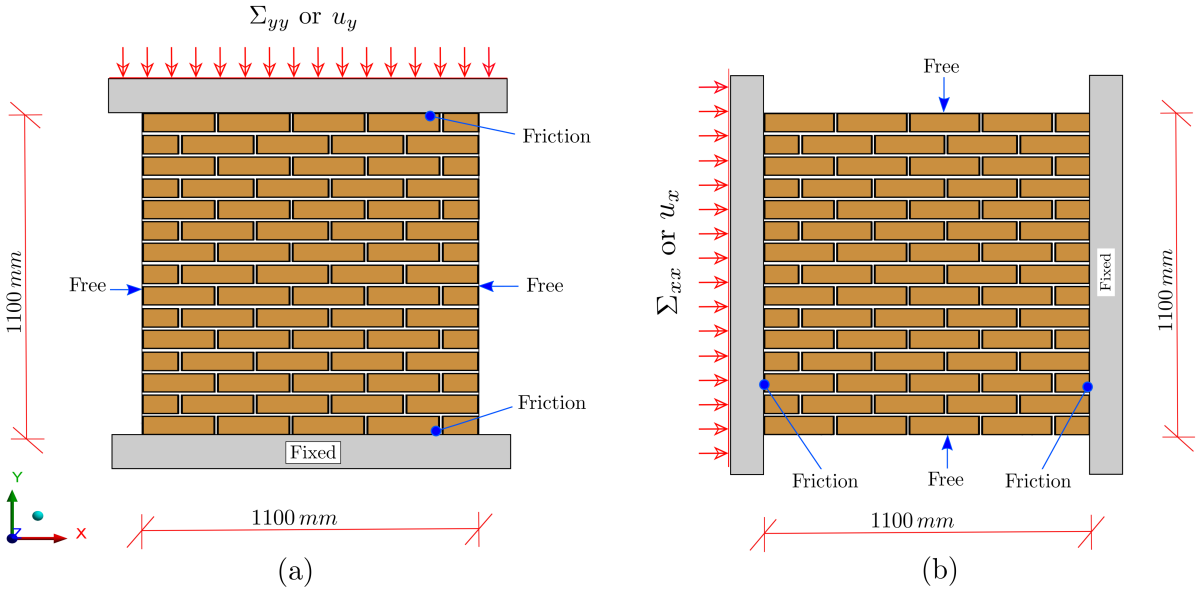

Figure 16: Schematics of masonry structures subjected to uniaxial compression in a) y- direction and b) x-direction: geometry and boundary conditions.

Gradual closure and reopening of joints in masonry structures subjected to uniaxial displacement LHU in the x and y directions are shown in figure 17 (points a to d are corresponding to points a to d in figure 18). Initially (figure17-a), all bed and head joints are open and the masonry structure is in pattern O (in both cases, x and y-LHU). In the case of y-LHU, the thickness of bed joints decreases gradually, with the increase of the applied displacement in the y direction, until joints closure while head joints are still open. Therefore, the masonry structure changes from pattern O to pattern B (figure17-b). During the holding step, bed joints remain closed (figure 17-c). Finally, during unloading, few bed joints near the fixed rigid plate reopen and, thus, the masonry structure change from pattern B back to pattern O. Similarly, in the case of x-LHU, with the gradual increase of the applied displacement in the x direction, head joints close gradually while bed joints remain open and, therefore, the masonry structure changes from pattern O to pattern H. Also, during holding step, there are no joints opening. However, during unloading, some head joints near the fixed rigid plate reopen and, as a result, there is a change to pattern O. In both cases (x and y-LHU), as expected, joints near the moving rigid plates close before those near the fixed rigid plate.

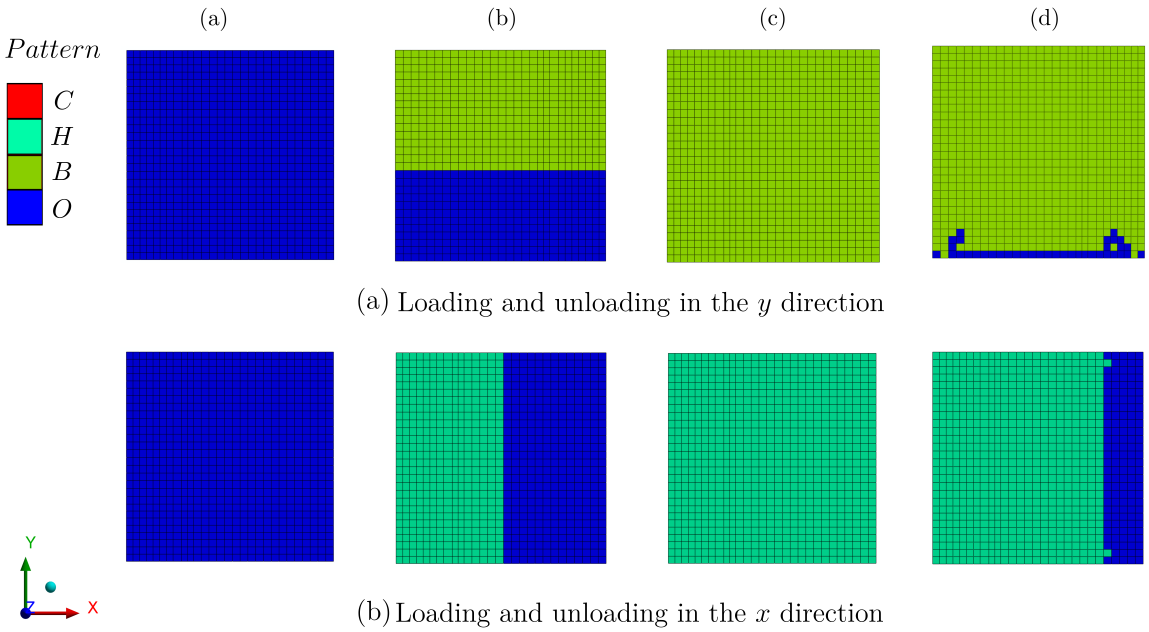

(a) Loading and unloading in the y direction

(b) Loading and unloading in the x direction

Figure 17: Gradual closure and reopening of joints in masonry wall subjected to uniaxial compression loading (displacement), holding and unloading in the y and x directions. (a) All joints are open (pattern O) at time = 0 seconds. (b) Gradual closure of joints due to the applied displacement. (c) All bed or head joints remain closed during the holding step. (d) Some joints reopen due to unloading.

Time variations of global displacement and stress of masonry structures subjected to constant uniaxial displacement LHU in the x and y directions are shown in figure 18. The global displacements are determined from those of the surfaces in contact with the moving rigid plates (i.e. $y = 1100\ mm$ in the case of $y-$ loading and $x = 0\ mm$ in the case of $x-$loading, see figure 16, and the stresses are calculated from the reaction forces of the moving rigid plates. During the first 180 sec., a displacement of 1.7 mm has been applied to the moving rigid plates (loading), then the displacement has been kept constant for the next 1000 sec. (holding) LHU and finally the rigid plates have been returned back to the initial position (unloading). During loading and holding steps, as can be seen from the figure 18, the global displacement of the masonry structure is equal to the displacement of the moving rigid plates (increases gradually to 1.7 mm during loading then remains constant during holding). However, during unloading, the masonry structure does not return back to its initial position and there is permanent deformation even after unloading (global displacement of the structure after unloading is around 1.5 mm). The reason for this behaviour is twofold; first, after unloading only few joints reopen and their final

thickness is very small as compared to the initial one (0.1 mm), second, the permanent deformation caused by viscoplasticity of the structure (see figures 19 and 20). As can be seen from figures 19 and 20, in the case of x-LHU, $E^{\text{vp}}_{\text{xx}}$ is higher as compared to $E^{\text{vp}}_{\text{yy}}$ in the case of y-LHU, because $\Sigma_{\text{xx}} > \Sigma_{\text{yy}}$ and according to equation 12, the viscoplastic strain rate increases with the increase of the stress.

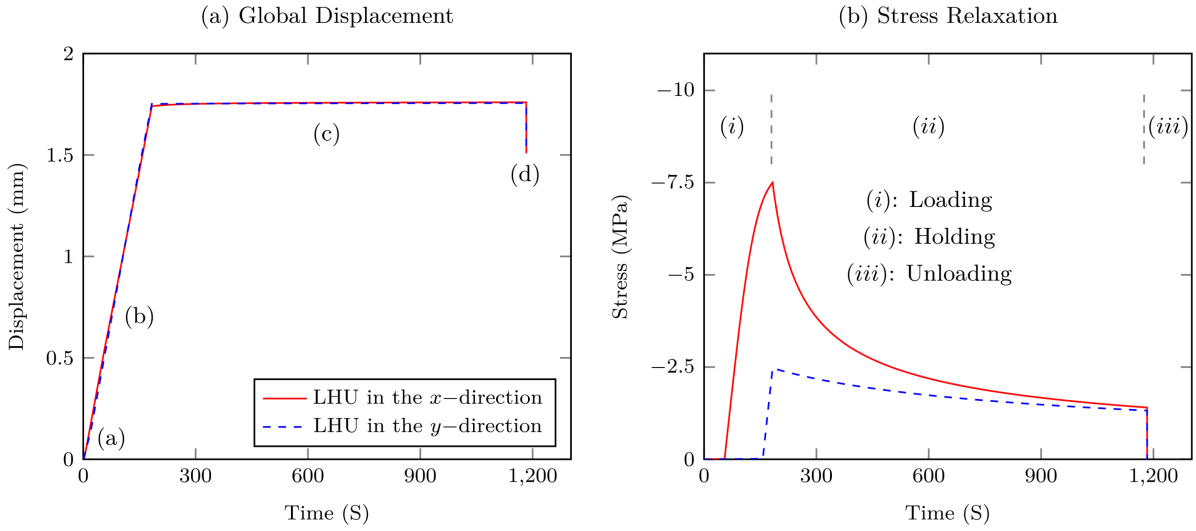

Figure 18: Time variations of a) global displacement and b) stress of masonry wall subjected to uniaxial compression displacement loading, holding and unloading in the x and the y directions. In both cases (x and y), the applied displacement load is equal. However, resulting stresses are different due to the orthotropic elastic-viscoplastic behaviour of the masonry structure.

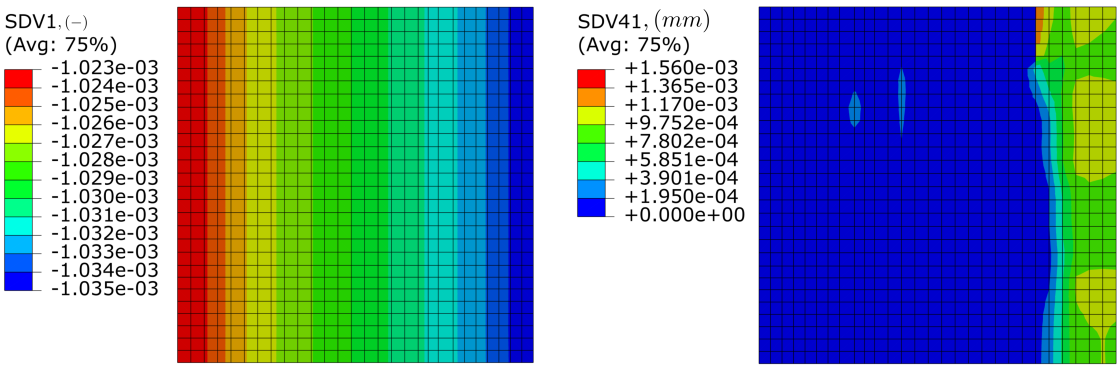

(a) E^{vp}_{xx} (b) g_{head}

Figure 19: Contours of viscoplastic strain and final head joints thickness (in mm) after unloading in mortarless masonry structure subjected to constant uniaxial compression displacement loading, holding and unloading in the x direction. After unloading, few head joints reopen ($g_{head} > 0$) and their thickness is very small as compared to the initial thickness (0.1 mm).

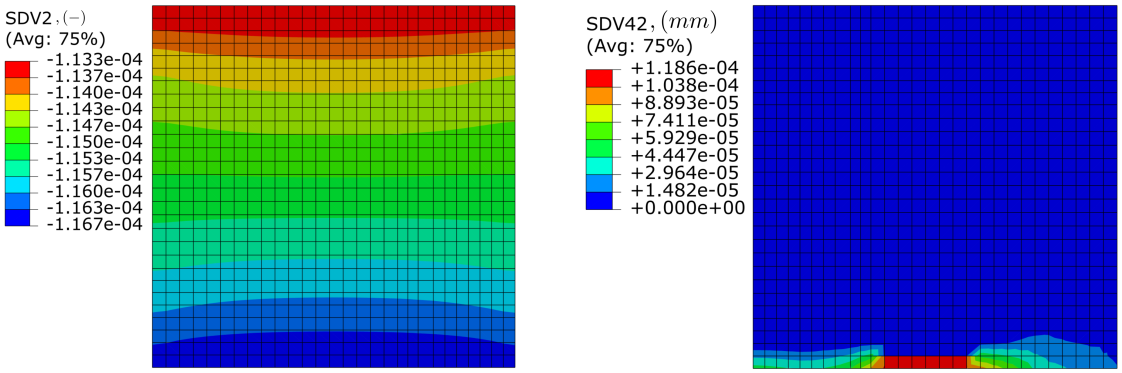

(a) E_{yy}^{vp} (b) g_{bed}

Figure 20: Contours of viscoplastic strain and final bed joints thickness (in mm) after unloading, in mortarless masonry structure subjected to constant uniaxial compression displacement loading, holding and unloading in the y direction. After unloading, few bed joints reopen ($g_{bed} > 0$) and their thickness is very small as compared to the initial thickness (0.1 mm).

Regarding time variations of stresses in the masonry structures, it has been noticed that, under the same applied displacement load (for both x and y-LHU), macroscopic stresses in the x direction (Σ_{xx}) are higher than stresses in the y direction (Σ_{yy}). This behaviour clearly illustrates the macroscopic orthotropic behaviour of the structure. In the case of x-LHU, during the first 75 seconds Σ_{xx} values are very small, because during this period gradual closure of head joints is occurring and the masonry structure is changing from pattern O to pattern B (i.e. material stiffness is very low). After closure of joints Σ_{xx} increases at higher rate to reach a peak of around 7.5 MPa by the end of loading step. Then during holding, a decrease in Σ_{xx} can be noticed due to stress relaxation and, finally, after unloading Σ_{xx} returns to zero. Similarly, in the case of y-LHU, at the first 170 seconds Σ_{yy} is very small as during this period bed and head joints are open (material stiffness is very small). Then, after bed joints closure, Σ_{yy} increases at higher rate to reach a peak of 2.5 MPa. Finally, a stress decay has been noticed due to stress relaxation.

It should be noted that, the peak in Σ_{xx} is much higher as compared to the peak in Σ_{yy}. Also, the time period during which Σ_{yy} is almost zero is longer as compared to this of Σ_{xx}. This can attributed to that the number of head joints is less as compared to the number of bed joints (4 head joints and 14 bed joints, see figure 16). Therefore, the closure of all head joints (due to gradual increase of applied x displacement) and the increase of macroscopic stiffness in the x direction of the material occurs faster as compared to

the closure of all bed joints (due to gradual increase of applied y displacement) and the increase of the material stiffness in the y direction.

Schematics of masonry structure geometry subjected to constant stress uniaxial compression in the x and y directions as well as the boundary conditions are presented in figure 16. Time variations of homogenized total strains in masonry structures subjected to constant uniaxial stress LHU conditions in the x, first loading case, and y, second loading case, directions are presented in figure 21. In both cases, the total strains in the normal directions to the surfaces of the dry joints are reported (i.e. $E^{\mathrm{t}}_{\mathrm{xx}}$ and $E^{\mathrm{t}}_{\mathrm{yy}}$). The loading steps are: first, applying constant stress of 1.5 MPa, second, holding for $50,000$ seconds and finally, unloading. Overall, it has been observed that total strains, in the loading direction, increases instantaneously due to load application, then increases at constant rate due to creep and finally it decreases slightly due to unloading. In addition, after load removal, the recovered strain (in the loading direction) is very small as compared to the instantaneous strain (due to the applied load at $t = 0$ sec). This can be attributed to that, first, during unloading, only few joints reopen and their final thickness is very small as compared to the initial joint thickness, second, the permanent deformation resulting from the viscoplastic behaviour of the structure.

Moreover, in the first loading case (x-LHU), the resulting instantaneous strain, in the loading direction ($E^{\mathrm{t}}_{\mathrm{xx}}$ at t = 0 seconds), is less as compared to the resulting instantaneous strain, in the loading direction ($E^{\mathrm{t}}_{\mathrm{yy}}$ at t = 0 seconds), in the second loading case (y-LHU). The reason for this is that the number of bed joints is higher than the number of head joints. Consequently, under the same applied stress level, all head joints close faster than bed joints and the increase of the macroscopic stiffness of the masonry in the x direction (during load application step) occurs faster as compared to the increase of the structure stiffness in the y direction. This leads to lower values of resulting instantaneous strain under the same applied stress level.

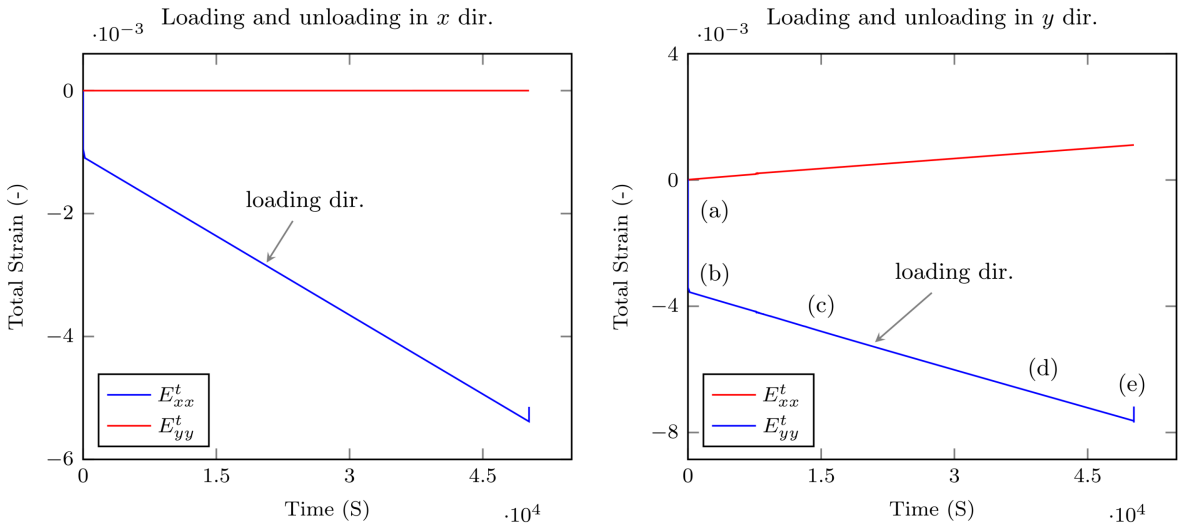

Figure 21: Time variations of macroscopic total strains in masonry structure subjected to constant stress loading, holding and unloading in the x and y directions. The total strains in the normal directions to the surfaces of the dry joints are reported. In both cases (x and y), the applied stress load is equal (1.5 MPa). However, resulting total strains are different due to the orthotropic elastic-viscoplastic behaviour of the masonry structure.

In the first loading case (x-LHU), gradual closure of joints is similar to those presented in figure 17-b (change from pattern O to pattern H due to load applications). As explained earlier, in the case of joint pattern H, the components of $\overline{\overline{\overline{C}}}^{\,e}$ and $\overline{\overline{\overline{N}}}$ in the y direction are equal to zero. It can bee seen from figure 21 that during the whole period (LHU), $E^{t}_{yy} = 0$ and, therefore, bed joints remain open. In the second loading case (y-LHU), bed joints close due to load application and the structure changes from pattern O to pattern B (see figure 22). Since the x components of $\overline{\overline{\overline{C}}}^{\,e}$ and $\overline{\overline{\overline{N}}}$ have values, it can be seen that E^{t}_{xx} increases with the passage of time. Consequently, as depicted in figure 22, head joints close gradually and the structure changes from pattern B to pattern C. The closure of head joints is mainly due to viscoplasticity (creep). At around 30,000 seconds, all head joints are closed and they remain closed until the end of the holding step. After unloading, some joints reopen and the recovered strain in the y direction is very small as compared to the instantaneous strain. In addition, there is no strain recovery in the x direction, because it is mainly caused by the viscoplasticity of the structure.

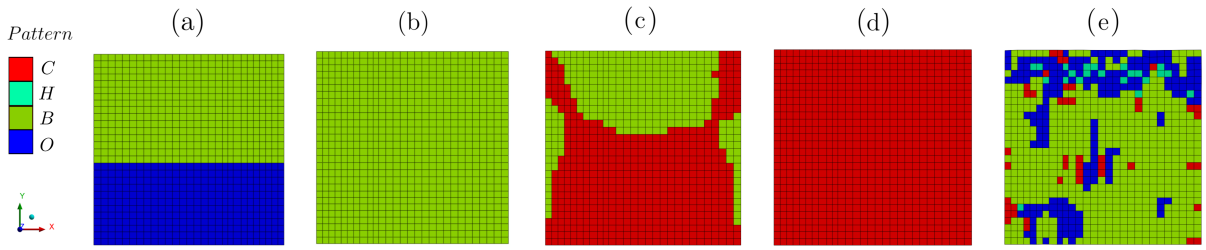

Figure 22: Gradual closure and reopening of joints in masonry wall subjected to 1.5 MPa constant stress LHU in the y direction. Points a to e are indicated in figure 21. (a) Gradual closure of bed joints due to the applied load. (b) All bed joints are closed by the end of the loading step. (c) Head joints close gradually due to creep. (d) All bed and head joints are closed. (e) Joints reopening due to unloading.

6 Conclusion

In the present study, computational homogenization of elastic viscoplastic refractory masonry with dry joints is performed. Four possible joint patterns are predefined based on the state of bed and head joints. Each joint pattern has different homogeneous elastic viscoplastic response which has been identified using nonlinear homogenization technique.

The homogenized elastic viscoplastic response of the first three patterns (patterns pattern O, pattern H and pattern B) is orthotropic due to the presence of open joints whereas, the homogenized response of the last joint pattern (pattern C) is isotropic and similar to the mechanical response of the base material of the bricks because all joints are closed. It has been shown that the presence of open joints leads to a significant reduction in the effective elastic stiffness of the structure and orthotropic viscoplastic behaviour.

Suitable macroscopic orthotropic constitutive laws are used to describe the homogenized elastic viscoplastic behaviour of the joint patterns. To assess the accuracy of the developed macro model, several finite element simulations of uniaxial, simple shear and biaxial loadings are carried out. Then, comparisons between average mechanical responses from the detailed micro model and the macro model are performed. Good agreements between the results from the micro and macro models are observed.

During operation, the masonry structure changes from one joint pattern to another leading to a change in the macroscopic elastic viscoplastic behaviour of the structure. This change is taken into account by employing suitable joints closure, reopening and

pattern transition criteria. The joints closure and reopening criteria are written in terms of macroscopic stresses and strains.

Several finite element simulations of mortarless masonry walls subjected to constant stress and constant strain uniaxial loading, holding and unloading are performed. It has been shown that the macroscopic elastic viscoplastic behaviour of mortarless masonry walls is orthotropic and nonlinear due to joints closure, reopening, creep and stress relaxation. In addition, after unloading only few joints reopen and the recovered strain is very small as compared to the instantaneous applied strain due to the viscoplastic behaviour of the structure and the final small joints thickness after unloading.

The presented numerical model takes into account the orthotropic, nonlinear, elastic viscoplastic behaviour of refractory masonry structures at high temperature and the presence of dry joints. It can be used to model and predict the homogeneous mechanical response of many high-temperature large sized industrial applications such as steel ladles and furnaces.

Funding

This work was supported by the funding scheme of the European Commission, Marie Skłodowska Curie Actions Innovative Training Networks in the frame of the project ATHOR - Advanced THermomechanical mOdelling of Refractory linings - 764987 Grant.

Acknowledgment

The authors are grateful to the Centre de Calcul Scientifique en région Centre Val de Loire (France) for the computation time and technical support.

Conflicts of interest

None to declare.

Appendix

Table A1: Effective elastic 4$^{\text{th}}$ order tensor of the four joint patterns of Magnesia Chromite refractory masonry wall at different temperatures.

Pattern	$\overline{\overline{\overline{\overline{C}}}}^{e}$ (MPa)																													
Temperature	20 °C						800 °C						1000 °C						1100 °C						1200 °C					
O	1	0	0	0	0	0	1	0	0	0	0	0	1	0	0	0	0	0	1	0	0	0	0	0	1	0	0	0	0	0
		1	0	0	0	0		1	0	0	0	0		1	0	0	0	0		1	0	0	0	0		1	0	0	0	0
			28500	0	0	0			15400	0	0	0			10600	0	0	0			9800	0	0	0			9100	0	0	0
				0	0	0				0	0	0				0	0	0				0	0	0				0	0	0
					11868	0					6413	0					4414	0					4081	0					3789	0
						11868						6413						4414						4081						3789
H	29670	0	5934	0	0	0	16041	0	3208	0	0	0	11041	0	2208	0	0	0	10208	0	2041	0	0	0	9479	0	1895	0	0	0
		1	0	0	0	0		1	0	0	0	0		1	0	0	0	0		1	0	0	0	0		1	0	0	0	0
			29670	0	0	0			16041	0	0	0			11041	0	0	0			10208	0	0	0			9479	0	0	0
				0	0	0				0	0	0				0	0	0				0	0	0				0	0	0
					11868	0					6413	0					4414	0					4081	0					3789	0
						11868						6413						4414						4081						3789
B	11557	2898	2891	0	0	0	6245	1565	1562	0	0	0	4298	1077	1075	0	0	0	3974	996	994	0	0	0	3690	925	923	0	0	0
		30397	6659	0	0	0		16425	3598	0	0	0		11305	2476	0	0	0		10452	2289	0	0	0		9705	2126	0	0	0
			30394	0	0	0			16423	0	0	0			11304	0	0	0			10451	0	0	0			9704	0	0	0
				8611	0	0				4653	0	0				3202	0	0				2961	0	0				2749	0	0
					7420	0					4009	0					2759	0					2551	0					2369	0
						11868						6413						4414						4081						3789
C	31666	7916	7916	0	0	0	17111	4277	4277	0	0	0	11777	2944	2944	0	0	0	10888	2722	2722	0	0	0	10111	2572	2572	0	0	0
		31666	7916	0	0	0		17111	4277	0	0	0		11777	2944	0	0	0		10888	2722	0	0	0		10111	2572	0	0	0
			31666	0	0	0			17111	0	0	0			11777	0	0	0			10888	0	0	0			10111	0	0	0
				11875	0	0				6416	0	0				4416	0	0				4083	0	0				3791	0	0
					11875	0					6416	0					4416	0					4083	0					3791	0
						11875						6416						4416						4083						3791

Table A2: Effective viscoplastic 4$^{\text{th}}$ order tensor of the four joint patterns of Magnesia Chromite refractory masonry wall at different temperatures.

Pattern	$\overline{\overline{\overline{\overline{N}}}}$ (−)											
Temperature	1100 °C						1200 °C					
O	0	0	0	0	0	0	0	0	0	0	0	0
		0	0	0	0	0		0	0	0	0	0
			1.27	0	0	0			2.01	0	0	0
				0	0	0				0	0	0
					3.79	0					6.03	0
						3.79						6.03
H	1.27	0	-0.6	0	0	0	2.01	0	-0.98	0	0	0
		0	0	0	0	0		0	0	0	0	0
			1.27	0	0	0			2.01	0	0	0
				0	0	0				0	0	0
					3.79	0					6.03	0
						3.79						6.03
B	4.24	-0.7	-0.6	0	0	0	6.61	-1.1	-0.92	0	0	0
		1.26	-0.6	0	0	0		2.02	-0.98	0	0	0
			1.27	0	0	0			2.01	0	0	0
				5.36	0	0				8.30	0	0
					6.21	0					9.63	0
						3.79						6.03
C	1.27	-0.6	-0.6	0	0	0	2.01	-0.98	-0.98	0	0	0
		1.27	-0.6	0	0	0		2.01	-0.98	0	0	0
			1.27	0	0	0			2.01	0	0	0
				3.79	0	0				6.03	0	0
					3.79	0					6.03	0
						3.79						6.03

References

[1] E. Blond, A. K. Nguyen, E. de Bilbao, T. Sayet, and A. Batakis, "Thermo-chemo-mechanical modeling of refractory behavior in service: Key points and new developments," *International Journal of Applied Ceramic Technology*, pp. 1–8, 2020.

[2] J. J. Coz Díaz, F. R. Mazón, P. J. García Nieto, and F. J. Suárez Domínguez, "Design and finite element analysis of a wet cycle cement rotary kiln," *Finite Elements in Analysis and Design*, vol. 39, no. 1, pp. 17–42, 2002.

[3] J. Qi, W. Yan, Z. Chen, S. Schafföner, W. Zhou, G. Li, and Q. Wang, "Preparation and characterization of microporous mullite-corundum refractory aggregates with

high strength and closed porosity," *Ceramics International*, vol. 46, pp. 8274–8280, apr 2020.

[4] S. Smets, S. Parada, J. Weytjens, G. Heylen, P. T. Jones, M. Guo, B. Blanpain, and P. Wollants, "Behaviour of magnesia-carbon refractories in vacuum-oxygen decarburisation ladle linings," *Ironmaking and Steelmaking*, vol. 30, no. 4, pp. 293–300, 2003.

[5] G. Wu, W. Yan, S. Schafföner, Y. Dai, B. Han, T. Li, S. Ma, N. Li, and G. Li, "A comparative study on the microstructures and mechanical properties of a dense and a lightweight magnesia refractories," *Journal of Alloys and Compounds*, vol. 796, pp. 131–137, aug 2019.

[6] E. Blond, N. Schmitt, F. Hild, P. Blumenfeld, and J. Poirier, "Effect of slag impregnation on thermal degradations in refractories," *Journal of the American Ceramic Society*, vol. 90, no. 1, pp. 154–162, 2007.

[7] J. Fruhstorfer, L. Schöttler, S. Dudczig, G. Schmidt, P. Gehre, and C. G. Aneziris, "Erosion and corrosion of alumina refractory by ingot casting steels," *Journal of the European Ceramic Society*, vol. 36, no. 5, pp. 1299–1306, 2016.

[8] K. Andreev, B. Luchini, M. Rodrigues, and J. L. Alves, "Role of fatigue in damage development of refractories under thermal shock loads of different intensity," *Ceramics International*, vol. 46, pp. 20707–20716, sep 2020.

[9] J. Chen, L. Chen, Y. Wei, N. Li, and S. Zhang, "Corrosion and penetration behaviors of slag/steel on the corroded interfaces of Al2O3-C refractories: Role of Ti3AlC2," *Corrosion Science*, vol. 143, pp. 166–176, oct 2018.

[10] Y. Dai, J. Li, W. Yan, and C. Shi, "Corrosion mechanism and protection of BOF refractory for high silicon hot metal steelmaking process," *Journal of Materials Research and Technology*, vol. 9, pp. 4292–4308, may 2020.

[11] Y. Zou, A. Huang, R. Wang, L. Fu, H. Gu, and G. Li, "Slag corrosion-resistance mechanism of lightweight magnesia-based refractories under a static magnetic field," *Corrosion Science*, vol. 167, p. 108517, may 2020.

[12] S. Samadi, S. Jin, D. Gruber, H. Harmuth, and S. Schachner, "Statistical study of compressive creep parameters of an alumina spinel refractory," *Ceramics International*, vol. 46, pp. 14662–14668, jul 2020.

[13] A. Gasser, K. Terny-Rebeyrotte, and P. Boisse, "Modelling of joint effects on refractory lining behaviour," *Proceedings of the Institution of Mechanical Engineers, Part L: Journal of Materials: Design and Applications*, vol. 218, no. 1, pp. 19–28, 2004.

[14] T. M. Nguyen, E. Blond, A. Gasser, and T. Prietl, "Mechanical homogenisation of masonry wall without mortar," *European Journal of Mechanics, A/Solids*, vol. 28, no. 3, pp. 535–544, 2009.

[15] M. Ali, T. Sayet, A. Gasser, and E. Blond, "Transient thermo-mechanical analysis of steel ladle refractory linings using mechanical homogenization approach," *Ceramics*, vol. 3, no. 2, pp. 171–189, 2020.

[16] T. Zahra and M. Dhanasekar, "Characterisation and strategies for mitigation of the contact surface unevenness in dry-stack masonry," *Construction and Building Materials*, vol. 169, pp. 612–628, apr 2018.

[17] T. Bui, A. Limam, V. Sarhosis, and M. Hjiaj, "Discrete element modelling of the in-plane and out-of-plane behaviour of dry-joint masonry wall constructions," *Engineering Structures*, vol. 136, pp. 277–294, 2017.

[18] G. G. Chewe Ngapeya and D. Waldmann, "Overcome of bed-joint imperfections and improvement of actual contact in dry-stacked masonry," *Construction and Building Materials*, vol. 233, p. 117173, 2020.

[19] N. A. Nodargi, C. Intrigila, and P. Bisegna, "A variational-based fixed-point algorithm for the limit analysis of dry-masonry block structures with non-associative Coulomb friction," *International Journal of Mechanical Sciences*, vol. 161-162, p. 105078, 2019.

[20] P. B. Lourenço, D. V. Oliveira, P. Roca, and A. Orduña, "Dry joint stone masonry walls subjected to in-plane combined loading," *Journal of Structural Engineering*, vol. 131, no. 11, pp. 1665–1673, 2005.

[21] J. A. Thamboo, T. Zahra, and R. Dhanasekar, "Development of design methodology for mortarless masonry system: Case study – a resettlement housing colony," *Journal of Building Engineering*, vol. 27, p. 100973, jan 2020.

[22] M. Martínez and S. Atamturktur, "Experimental and numerical evaluation of reinforced dry-stacked concrete masonry walls," *Journal of Building Engineering*, vol. 22, pp. 181–191, 2019.

[23] H. Smoljanović, Ž. Nikolić, and N. Živaljić, "A finite-discrete element model for dry stone masonry structures strengthened with steel clamps and bolts," *Engineering Structures*, vol. 90, pp. 117–129, 2015.

[24] G. Tempesta and S. Galassi, "Safety evaluation of masonry arches. A numerical procedure based on the thrust line closest to the geometrical axis," *International Journal of Mechanical Sciences*, vol. 155, pp. 206–221, may 2019.

[25] G. G. Chewe Ngapeya and D. Waldmann, "Experimental and analytical analysis of the load-bearing capacity Pu of improved dry-stacked masonry," *Journal of Building Engineering*, vol. 27, p. 100927, 2020.

[26] D. Foti, V. Vacca, and I. Facchini, "DEM modeling and experimental analysis of the static behavior of a dry-joints masonry cross vaults," *Construction and Building Materials*, vol. 170, pp. 111–120, may 2018.

[27] H. Smoljanović, N. Živaljić, Ž. Nikolić, and A. Munjiza, "Numerical analysis of 3D dry-stone masonry structures by combined finite-discrete element method," *International Journal of Solids and Structures*, vol. 136-137, pp. 150–167, apr 2018.

[28] C. Casapulla and L. U. Argiento, "In-plane frictional resistances in dry block masonry walls and rocking-sliding failure modes revisited and experimentally validated," *Composites Part B: Engineering*, vol. 132, pp. 197–213, 2018.

[29] F. Portioli and L. Cascini, "Large displacement analysis of dry-jointed masonry structures subjected to settlements using rigid block modelling," *Engineering Structures*, vol. 148, pp. 485–496, 2017.

[30] S. Allaoui, A. Rekik, A. Gasser, E. Blond, and K. Andreev, "Digital image correlation measurements of mortarless joint closure in refractory masonries," *Construction and Building Materials*, vol. 162, pp. 334–344, 2018.

[31] K. Andreev, S. Sinnema, A. Rekik, S. Allaoui, E. Blond, and A. Gasser, "Compressive behaviour of dry joints in refractory ceramic masonry," *Construction and Building Materials*, vol. 34, pp. 402–408, 2012.

[32] A. Hou, S. Jin, H. Harmuth, and D. Gruber, "A Method for Steel Ladle Lining Optimization Applying Thermomechanical Modeling and Taguchi Approaches," *Jom*, vol. 70, no. 11, pp. 2449–2456, 2018.

[33] "ATHOR Refractory Linings - ETN ATHOR." `https://www.etn-athor.eu/,accessed:2020-05-15.`

[34] J. Lemaitre and J.-L. Chaboche, *Mechanics of Solid Materials*. Cambridge University Press, 1990.

[35] E. Blond, N. Schmitt, F. Hild, P. Blumenfeld, and J. Poirier, "Modelling of high temperature asymmetric creep behavior of ceramics," *Journal of the European Ceramic Society*, vol. 25, no. 11, pp. 1819–1827, 2005.

[36] M. Ali, T. Sayet, A. Gasser, and E. Blond, "Thermomechanical modelling of refractory mortarless masonry wall subjected to biaxial compression," in *UNITECR*, (Yokohama, Japan), 2019.

[37] A. Rekik and A. Gasser, "Numerical homogenization model for effective creep properties of microcracked masonry," *International Journal of Solids and Structures*, vol. 102-103, pp. 297–320, 2016.

[38] M. Tsuda, E. Takemura, T. Asada, N. Ohno, and T. Igari, "Homogenized elastic-viscoplastic behavior of plate-fin structures at high temperatures: Numerical analysis and macroscopic constitutive modeling," *International Journal of Mechanical Sciences*, vol. 52, no. 5, pp. 648–656, 2010.

[39] M. Tsuda and N. Ohno, "Duplex model for homogenized elastic-viscoplastic behavior of plate-fin structures at high temperatures," *International Journal of Plasticity*, vol. 27, no. 10, pp. 1560–1576, 2011.

[40] K. Goto, M. Arai, T. Matsuda, and G. Kubo, "Elasto-viscoplastic analysis for negative through-the-thickness Poisson's ratio of woven laminate composites based on homogenization theory," *International Journal of Mechanical Sciences*, vol. 146-147, pp. 455–461, 2018.

[41] E. Tikarrouchine, G. Chatzigeorgiou, Y. Chemisky, and F. Meraghni, "Fully coupled thermo-viscoplastic analysis of composite structures by means of multi-scale three-dimensional finite element computations," *International Journal of Solids and Structures*, vol. 164, pp. 120–140, 2019.

[42] Z. Xia, Y. Zhang, and F. Ellyin, "A unified periodical boundary conditions for representative volume elements of composites and applications," *International Journal of Solids and Structures*, vol. 40, no. 8, pp. 1907–1921, 2003.

[43] S. L. Omairey, P. D. Dunning, and S. Sriramula, "Development of an ABAQUS plugin tool for periodic RVE homogenisation," *Engineering with Computers*, vol. 35, no. 2, pp. 567–577, 2019.

[44] P. Henyš, L. Čapek, and J. Březina, "Comparison of current methods for implementing periodic boundary conditions in multi-scale homogenisation," *European Journal of Mechanics, A/Solids*, vol. 78, no. July, p. 103825, 2019.

[45] J. N. Reddy, *Mechanics of laminated composite plates and shells: theory and analysis*. CRC press, 2003.

[46] A. Iltchev, V. Marcadon, S. Kruch, and S. Forest, "Computational homogenisation of periodic cellular materials: Application to structural modelling," *International Journal of Mechanical Sciences*, vol. 93, pp. 240–255, 2015.

[47] R. Hill, "The essential structure of constitutive laws for metal composites and polycrystals," *Journal of the Mechanics and Physics of Solids*, vol. 15, no. 2, pp. 79–95, 1967.

[48] M. Hori and S. Nemat-Nasser, "On two micromechanics theories for determining micro-macro relations in heterogeneous solids," *Mechanics of Materials*, vol. 31, no. 10, pp. 667–682, 1999.

[49] F. Fritzen, S. Forest, T. Böhlke, D. Kondo, and T. Kanit, "Computational homogenization of elasto-plastic porous metals," *International Journal of Plasticity*, vol. 29, no. 1, pp. 102–119, 2012.

[50] T. Matsuda, N. Ohno, H. Tanaka, and T. Shimizu, "Effects of fiber distribution on elastic-viscoplastic behavior of long fiber-reinforced laminates," *International Journal of Mechanical Sciences*, vol. 45, no. 10, pp. 1583–1598, 2003.

[51] T. T. Molla, K. Kwok, and H. L. Frandsen, "Efficient modeling of metallic interconnects for thermo-mechanical simulation of SOFC stacks: Homogenized behaviors and effect of contact," *International Journal of Hydrogen Energy*, vol. 41, no. 15, pp. 6433–6444, 2016.

[52] N. Ohno, K. Narita, and D. Okumura, "Homogenized elastic-viscoplastic behavior of plate-fin structures with two pore pressures," *International Journal of Mechanical Sciences*, vol. 86, pp. 18–25, 2014.

[53] N. Ohno, K. Ikenoya, D. Okumura, and T. Matsuda, "Homogenized elastic-viscoplastic behavior of anisotropic open-porous bodies with pore pressure," *International Journal of Solids and Structures*, vol. 49, no. 19-20, pp. 2799–2806, 2012.

[54] Z. Xue and J. W. Hutchinson, "Constitutive model for quasi-static deformation of metallic sandwich cores," *International Journal for Numerical Methods in Engineering*, vol. 61, no. 13, pp. 2205–2238, 2004.

[55] *Abaqus Documentation, ABAQUS/standard: User's Manual*. 1998.

[56] A. Triessnig, H. Studnicka, and T. Prietl, "Determination of Thermo-Mechanical Properties at the RHI Refractories Technology Center Leoben," *RHI Bulletin*, no. 1, pp. 33–37, 2006.

[57] T. Prietl, H. Antrekowitsch, A. Triessnig, H. Studnicka, and A. Filzwieser, "The evaluation of refractory linings thermo-mechanical properties," *Proceedings - European Metallurgical Conference, EMC 2005*, vol. 3, pp. 1099–1112, 2005.

[58] T. Prietl, *Determination of material-specific parameters of refractory materials and linings under uniaxial and biaxial load conditions for the non-ferrous metal industry, in German*. PhD thesis, Montanuniversität Leoben, 2006.

[59] S. Jin, H. Harmuth, and D. Gruber, "Compressive creep testing of refractories at elevated loads-Device, material law and evaluation techniques," *Journal of the European Ceramic Society*, vol. 34, no. 15, pp. 4037–4042, 2014.